minerals

MDPI

Article

Thrust Structure and Bidirectional Paleocurrent in the Jingzhushan Formation during the Late Cretaceous in the Nyima Basin, Tibet Plateau, China: Approach of Magnetic Fabric and Zircon Chronology

Qinglong Chen [1,*], Xin Cheng [1], Feifei Huo [1,2], Yanan Zhou [1], Nan Jiang [1,3], Bitian Wei [1], Yuchun Liu [1], Baofeng Wang [1,4], Pengxiang Xu [1,4], Dongmeng Zhang [1], Longyun Xing [1], Teng Li [1], Feifan Liu [1], Jingyue Wu [1], Jiawei Wang [1] and Hanning Wu [1,*]

[1] State Key Laboratory of Continental Dynamics, Department of Geology, Northwest University, Xi'an 710069, China
[2] College of Engineering, Zunyi Normal University, Zunyi 563006, China
[3] College of Petrol and Environment Engineering, Yan'an University, Yan'an 716000, China
[4] Gansu Provincial Coal Geological Exploration Institute, Lanzhou 730000, China
* Correspondence: chenqinglong@stumail.nwu.edu.cn (Q.C.); wuhn2506@nwu.edu.cn (H.W.)

Abstract: (1) Background: The widely developed thrust structures in the Jingzhushan Formation of late Cretaceous in Nyima Basin are related to the collision which leads to orogeny between the Lhasa and Qiangtang blocks. Clarifying the tectonic properties of the Nyima Basin is of great significance to characterize the evolution of the collision between the Lhasa block and the Qiangtang block. (2) Methods: Combined with mineralogy and petrology and U-Pb zircon dating of extrusive rocks, a detailed magnetic fabric test and rock magnetic experiment were carried out on the red sandstones of the Late Cretaceous Jingzhushan Formation in Nyima Basin. (3) Results: The sedimentary magnetic fabrics developed at the three sampling locations in the southern part of the basin are related to paleocurrents. The strained magnetic fabrics developed at one sampling site in the north, including pencil-like fabrics and tensile linear fabrics, are related to SE-NW tectonic stress. The average magnetic susceptibility value of the strained fabric with sandstone is lower than that of the sedimentary fabric, and its size is controlled by mica paramagnetic minerals. Ferromagnetic minerals are magnetite or hematite. In addition, the age of sandstone in the Jingzhushan Formation from the Nyima Basin matches the age of the eruptive rock in the Jingzhushan Formation from Coqen Basin, which is 92 Ma. (4) Conclusions: The strained fabric is developed near the thrust fault, which can explain the widely developed thrust structures in the basin. The Nyima Basin of the Jingzhushan Formation in the Late Cretaceous was an ocean-continent transitional foreland basin developed under the background of arc-arc "soft collision".

Keywords: Nyima Basin; the Jingzhushan Formation; the Late Cretaceous; thrust structure; magnetic fabric; zircon U-Pb dating; arc-arc "soft collision"

Citation: Chen, Q.; Cheng, X.; Huo, F.; Zhou, Y.; Jiang, N.; Wei, B.; Liu, Y.; Wang, B.; Xu, P.; Zhang, D.; et al. Thrust Structure and Bidirectional Paleocurrent in the Jingzhushan Formation during the Late Cretaceous in the Nyima Basin, Tibet Plateau, China: Approach of Magnetic Fabric and Zircon Chronology. *Minerals* **2022**, *12*, 1225. https://doi.org/10.3390/min12101225

Academic Editor: Frederick Lin Sutherland

Received: 29 July 2022
Accepted: 21 September 2022
Published: 28 September 2022

1. Introduction

The Tibet Plateau was formed during the combination of a series of land blocks and the southern margin of the Eurasian continent [1–8]. Among them, the Lhasa Block and the Qiangtang Block experienced tectonic events such as oceanic subduction and extinction, ocean-continent transition, arc-continent collision and continental-continental collision during the Early and Middle Jurassic to Late Cretaceous. Red beds exposed in the Nyima Basin during the Jingzhushan Formation of the Late Cretaceous marks the end of the subduction between the Bannu Oceanic Basin and the South Qiangtang Block, and the transition to intracontinental collision.

According to the collision orogeny theory, collisions are divided into continental-continental "hard collision" and continental-arc "soft collision" [9–11], and the corresponding collision zones are "superimposed zones" [12–14] and "docking zones", respectively. Based on this, there are many controversies about the tectonic evolution on the Nyima Basin, mainly on collision types, basin properties, tectonic types, and molasse types, etc. Controversies in collision types include continental-continental "hard collision", arc-continental "soft collision", and arc-arc "soft collision". Basin properties include strike-slip extensional basin [15,16], faulted basin [17,18] and back-arc foreland basin [19,20].

The strike-slip extensional basin is related to the dextral strike-slip and derived extension of the Bangong-Nujiang suture. The faulted basin is formed in the tectonic uplift activity in the background of continental collision. The back-arc foreland basin is related to the northward subduction under the background of the Bangong-Nujiang Tethys Ocean during the Late Jurassic to Early Cretaceous. In the division of structural types, there are two types of extrusion and extension. At the same time, molasse deposits during the Jingzhushan Formation are further divided into ocean-continent transition and basin-mountain coupling. The division of different basin properties and tectonic types is related to the degree of evolution from ocean-continent collision to continental-continental collision. Therefore, it is of great significance for limiting the tectonic evolution process of plate collision and combination, which include constraining the tectonic properties of the Nyima Basin in the Late Cretaceous and clarifying the collision mode and degree between the Lhasa Block and the Qiangtang Block.

This paper mainly studies the magnetic fabric of the sandstone in the Jingzhushan Formation from the Nyima Basin. Combined with rock magnetism, mineralogy and petrology and zircon U-Pb dating, we explain the widely developed thrust structures in the basin. Correspondingly, the tectonic properties of the basin are obtained, and the collision process is described.

Magnetic fabrics are studied for five strain fabrics of sedimentary rocks from initial deposition to stress deformation. Sedimentary fabrics represent sedimentary events related to paleocurrents, and strain fabrics represent the stress deformation of tectonic stress to original sedimentary fabrics. The strained magnetic fabric includes initial deformation fabric, pencil-like fabric, weak cleavage fabric, strong cleavage fabric and tensile linear fabric from weak to strong [21–25]. The six magnetic fabrics reflect the diagenetic characteristics of mineral deposits and the strain characteristics of tectonic deformation. Using the anisotropy of magnetic susceptibility (AMS) analysis technique, the sedimentary characteristics and the strain characteristics of magnetic-bearing minerals are analyzed, so as to realize the research on the direction of paleocurrent [26,27] and tectonic stress [21], etc.

2. Geological Background

The study area is located on the northern margin of the Lhasa Block, and on the south side of the Bangong-Nujiang suture. It is located in the middle of the Bangong-Nujiang suture zone, to Dagze Co as the center, and is near the east-west direction of the spindle-shaped foreland basin (Figure 1a). East-west trending thrust faults developed within the basin and thrust nappe structures are widely seen [28]. The broad Nyima Basin extends northward to the Chaburaga-Gobao Ekong Fault Zone, southward to the Raja-Songorj Fault Zone, eastward to the Lompola Basin, and westward to the Ojiu Basin [29]. In a narrow sense, the Nyima Basin is divided into a central uplift zone and source zones north and south.

The sedimentary stratigraphy within the basin ranges from the Wugga Formation (T_3w) and the Chokhara Group (T_3Q) in the Late Triassic to the Kangto Formation (ENk), the Oxburgh Formation (E1-2n) in the Palaeocene and the Quaternary (Q). The main outcrops of Middle to Late Jurassic-Cretaceous strata are the Mugagangri Mélange (MMJ), the Shamuro Formation (J_3s) with volcanic arc facies, the Tukarj Formation (J_3t) with shallow marine platform facies, the Doni Formation (K_1d) with sea-land transitional facies, the Langshan Formation ($K_{1\text{-}2}l$) with marina neritic facies and the Jingzhushan Formation

(K_2j) with river-lake facies (Figure 1b). The Langshan Formation ($K_{1\text{-}2}l$) is usually taken as the highest marine formation, indicating the end of marine deposition and the completion of the ocean-land transition.

Subsequently, widespread outcrop of molasse red beds in the Jingzhushan Formation marks the formal onset of terrestrial deposition. The tectonic evolution and sedimentary development of the Nyima Basin have extensive connections with the Lhasa Block, the South Qiangtang Block and the Nierong-Amdo micro-continent (Figure 1c).

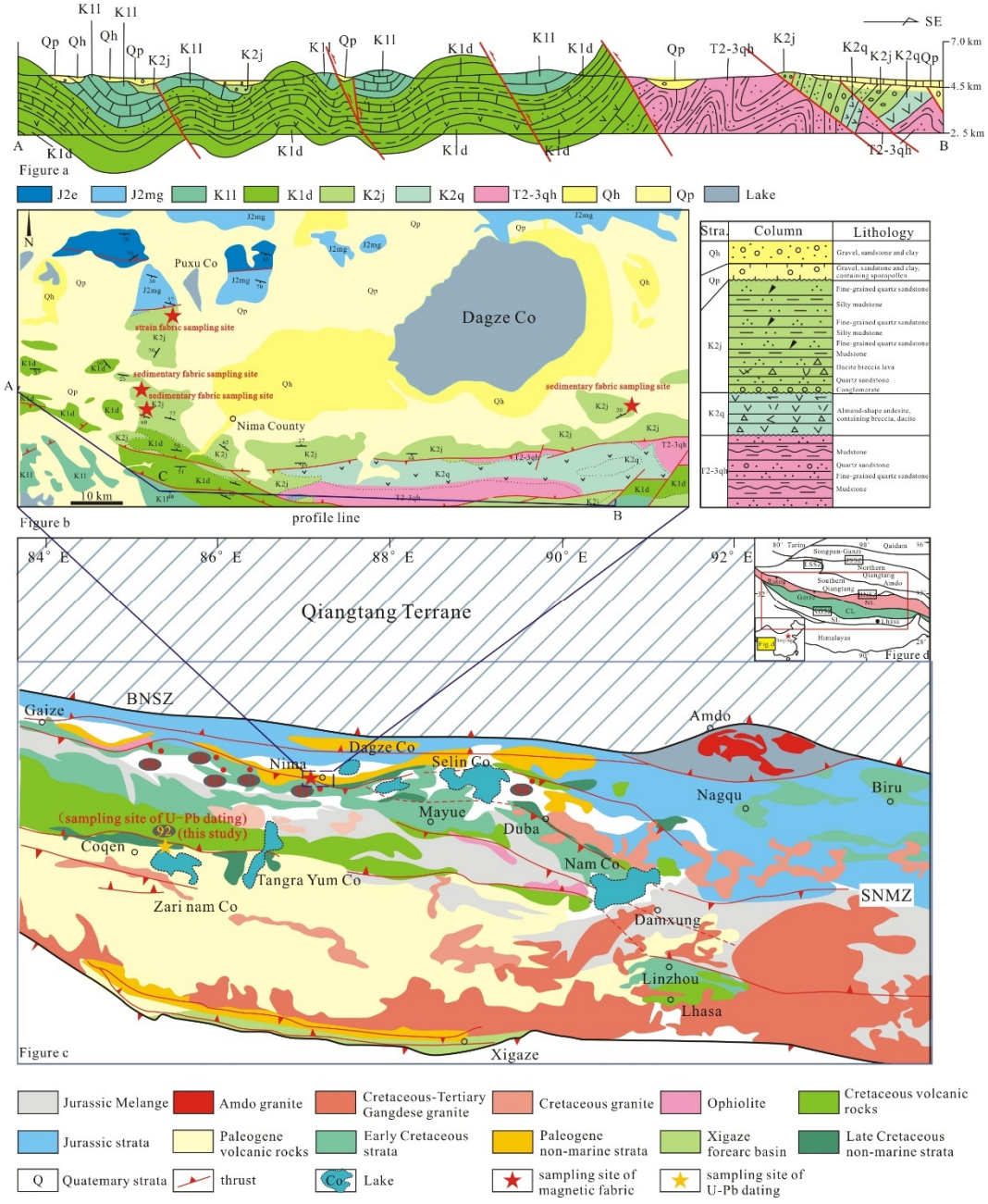

Figure 1. Geological overview map of the study area. (**a**) Distribution of outcrops and location of sampling sites in the study area of Nyima Basin. Contains stratigraphic column and tectonic sections of the study area. (**b**) Distribution of outcrops and location of sampling sites in the study area of Nyima Basin. Contains stratigraphic column and tectonic sections of the study area. (**c**) Distribution of outcrops in the Bangong-Nujiang suture zone and the northern margin of Lhasa. (**d**) Location of the study area.

3. Sample Collection and Test Method

The samples for the detailed magnetic fabric study are all from the red-bed sandstones in the Jingzhushan Formation of Late Cretaceous in the Nyima Basin. A total of four sampling locations are located in the northwest, west and east of the Nyima County (Figure 1c). The coordinates of the profile positions are 31°53′34″ N, 87°10′11″ E; 31°47′07″ N, 87°10′56″ E; 31°47′33″ N, 87°08′36″ E and 31°48′40″ N, 87°41′17″ E respectively. The lithology of the samples is mainly silty mudstone and argillaceous siltstone. Samples sites in the northwest of the county are predominantly red in color. Samples sites in the east-west of the county are relatively darker, with a predominantly puce color. There were 39 samples from the northern sampling location, 28 and 92 from the two western sampling locations, and 72 from the eastern sampling location.

In addition, the zircon U-Pb dating samples from the Jingzhushan Formation are purple-red volcanic extrusive rocks in the Coqen Basin, 180 km southwest of the Nyima Basin. The profile is located in the north shore of Zari nam Co, and coordinate position is 31°07′13″ N, 85°25′39″ E (Figure 1b). The reason why the object of U-Pb zircon dating research is the volcanic rock of the Jingzhushan Formation from the Coqen Basin and not the red bed of the Jingzhushan Formation from the Nyima Basin is as follows: In the Nyima Basin, there are already more age data from the Jingzhushan Formation, and most of the data objects are sandstones, but there are few volcanic rocks in the Jingzhushan Formation. All samples were drilled in the field with a portable petrol drill; they were also oriented and sampled with an orienter and magnetic compass and then cut into standard cylindrical samples 2.2 cm high.

Magnetic fabric testing and rock magnetism experiments of samples were completed at the State Key Laboratory of Continental Dynamics, Northwestern University. The magnetic fabric analysis was carried out using a Kappabridge susceptibility meter (MFK1-FB, test field strength 300 $A \cdot m^{-1}$, detection limit 2×10^{-8} SI, test accuracy 1%) from Advanced Geoscience Instruments Company (AGICO), Czech Republic, to test the anisotropy of magnetic susceptibility at low field (temperature 298 K, operating frequency 975 Hz) at room temperature. The test results were processed using Anisoft 4.2 software (AGICO, Brno, Czech Republic) and are shown in Table 1.

Rock magnetic experiments are isothermal remanence (IRM) experiments, which use a plus magnetic curve with positive field and degeneration curve with reverse field. This determines the type of magnetic minerals in the sample according to the characteristics of the increasing field. After obtaining saturation isothermal remanence (SIRM), reverse field cleaning was applied to the sample. An ASC IM-10-30 pulse magnetic instrument was used to add magnetic field, which was measured by a JR-6A dual-speed rotation magnetic meter. At the same time, the experiments of systemic thermal demagnetization are added, and the curve of thermal demagnetization is used to comprehensively determine the type of magnetic minerals. TD-48 thermal demagnetization furnace is used for sample demagnetization with heating. The temperature interval of the low temperature stage (0 °C–300 °C) is 50 °C–100 °C, and the temperature interval of the high temperature stage (300 °C–680 °C) is 15 °C–25 °C. When the temperature of the magnetic mineral is near the Curie temperature, the interval is 5 °C–10 °C. The test of residual magnetic component for sandstone samples was performed with the 2G-755 low-temperature superconducting magnetometer, and the sample of extrusive rock was tested on the JR6 two-speed rotating magnetometer.

The test of zircon U-Pb isotope dating was completed at Nanjing Hongchuang Geological Exploration Technology Service Co., Ltd. Zircon crystals with a clear external ring and intact internal structure were analyzed. The U-Th-Pb isotope dating was performed using the international standard zircon 91500 and Australian zircon GJ-1 as external standards.

Table 1. Magnetic susceptibility parameters of the red-bed samples in the Jingzhushan Formation from the Nyima Basin in room temperature (RT).

Sampling	N	Km	L	F	Pj	T	K1	K2	K3
KJ01-03	9	1.04×10^{-4}	1.002	1.001	1.004	−0.249	156.2/84.5	252.4/0.6	342.4/5.5
KJ04	7	1.63×10^{-4}	1.010	1.001	1.013	−0.759	206.5/4.8	115.5/11.0	319.7/78.0
KJ05	6	1.85×10^{-4}	1.009	1.003	1.013	−0.512	214.8/5.4	122.5/23.1	317.1/66.2
KJ06	6	1.72×10^{-4}	1.010	1.004	1.014	−0.367	211.1/9.1	98.9/66.9	304.6/21.0
KJ07	5	1.68×10^{-4}	1.013	1.002	1.016	−0.719	209.6/10.0	301.2/9.3	73.6/76.3
KJ08	6	1.63×10^{-4}	1.005	1.002	1.008	−0.275	52.4/52.1	252.6/36.1	155.3/9.9
North sampling point (average)	39	1.55×10^{-4}	1.008	1.002	1.011	−0.463	32.3/7.9	137.6/62.3	298.4/26.4
KJ24	6	1.11×10^{-4}	1.006	1.008	1.014	0.192	57.0/11.2	324.1/14.7	182.9/71.4
KJ32	12	3.58×10^{-4}	1.010	1.049	1.063	0.657	128.8/5.8	33.8/40.5	225.5/48.9
KJ35	10	1.59×10^{-4}	1.003	1.006	1.009	0.222	56.2/14.2	322.3/15.2	187.5/68.9
South sampling point (average)	28	2.34×10^{-4}	1.007	1.025	1.033	0.402	120.1/8.2	24.5/34.1	221.8/54.6
WKJ01	11	3.09×10^{-4}	1.009	1.016	1.025	0.290	298.8/11.3	29.3/2.6	132.0/78.4
WKJ02	7	2.55×10^{-4}	1.008	1.015	1.024	0.218	114.6/2.9	23.9/14.7	215.4/75.0
WKJ03	10	2.74×10^{-4}	1.008	1.024	1.034	0.458	288.5/10.5	21.7/17.1	168.3/69.8
WKJ04	5	3.96×10^{-4}	1.008	1.027	1.037	0.527	298.0/2.9	29.3/23.7	201.4/66.1
WKJ05	14	3.56×10^{-4}	1.009	1.018	1.028	0.263	101.3/6.1	10.9/3.3	252.8/83.1
WKJ06	8	4.62×10^{-4}	1.009	1.021	1.031	0.369	97.8/0.3	187.8/4.4	3.6/85.6
WKJ07	9	4.05×10^{-4}	1.014	1.025	1.040	0.306	134.2/12.2	43.3/4.4	293.7/76.9
WKJ08	9	4.39×10^{-4}	1.012	1.031	1.045	0.443	290.8/7.2	21.5/5.6	148.9/80.8
WKJ09	9	2.94×10^{-4}	1.011	1.015	1.027	0.129	281.8/10.9	11.9/0.6	105.0/79.0
WKJ10	10	5.42×10^{-4}	1.009	1.029	1.040	0.517	92.4/13.5	359.8/10.6	232.8/72.7
West sampling point (average)	92	3.72×10^{-4}	1.010	1.022	1.033	0.344	288.4/0.7	18.5/8.3	193.6/81.7
EKJ01	15	1.42×10^{-4}	1.009	1.022	1.033	0.462	214.8/3.9	304.8/0.6	43.9/86.0
EKJ02	20	2.45×10^{-4}	1.013	1.042	1.059	0.465	197.3/3.4	107.1/4.6	323.9/84.3
EKJ03	11	1.50×10^{-4}	1.010	1.021	1.032	0.342	39.1/7.0	129.9/6.4	262.0/80.5
EKJ04	19	2.07×10^{-4}	1.007	1.022	1.031	0.457	56.4/3.1	147.1/13.0	313.4/76.6
EKJ05	7	1.89×10^{-4}	1.006	1.012	1.018	0.299	242.3/0.4	152.2/8.3	335.0/81.6
East sampling point (average)	72	1.94×10^{-4}	1.010	1.026	1.038	0.427	214.4/1.2	124.3/6.4	314.6/83.5

4. Results

4.1. Mineralogy and Petrology

The samples used for zircon U-Pb dating in the Coqen Basin are volcanic extrusive rocks, in which there are crystal pyroclasts with different sizes and sharp edges (Figure 2). The samples used in the study of magnetic fabrics in the Nyima Basin are glutenite accumulations produced by typical continental orogens. The types of rock debris include normal sedimentary debris, extrusive debris, and metamorphic debris. The accumulation of debris with different origins can indicate the unified diagenetic process after denudation in the Jingzhushan Formation of the Late Cretaceous. The debris types of the samples collected at the west side of Nyima County are mainly extrusive rock debris. The minerals slices are red-brown or opaque due to the presence of much magnetite, and the quartz grains are filled with magnetite or dark minerals (Figure 3). The mineral type is mainly quartz, with a small amount of feldspar and white mica. Quartz grains typically originate from "recycling" detrital quartz of parent rock, usually containing gas-liquid inclusions. There is an enlarged quartz edge at the edge of the particle, and the enlarged edge is usually irregular due to abrasion during handling. Some are also derived from volcanic quartz, with the shape of embayed margins and intragranular micro-fractures.

Quartz conglomerate shows an irregular shape without cleavage and two crystal structures. The interference color of white mica is bright under the polarising microscope. Biotite is decomposed into chlorite and magnetite. Under the polarising microscope, it is

multicolored, mainly black or dark brown, with a small amount of green. In addition to extrusive debris, there is also a small quantity of metamorphic debris. Metamorphic debris includes polycrystalline quartz and sericite phyllite. The crystal grains of polycrystalline quartz are in suture contact, and the suture lines are complex in bending, generally multi-stage crystallization, and the mineral grains after crystallization are significantly larger than other single quartz grains (Figure 3).

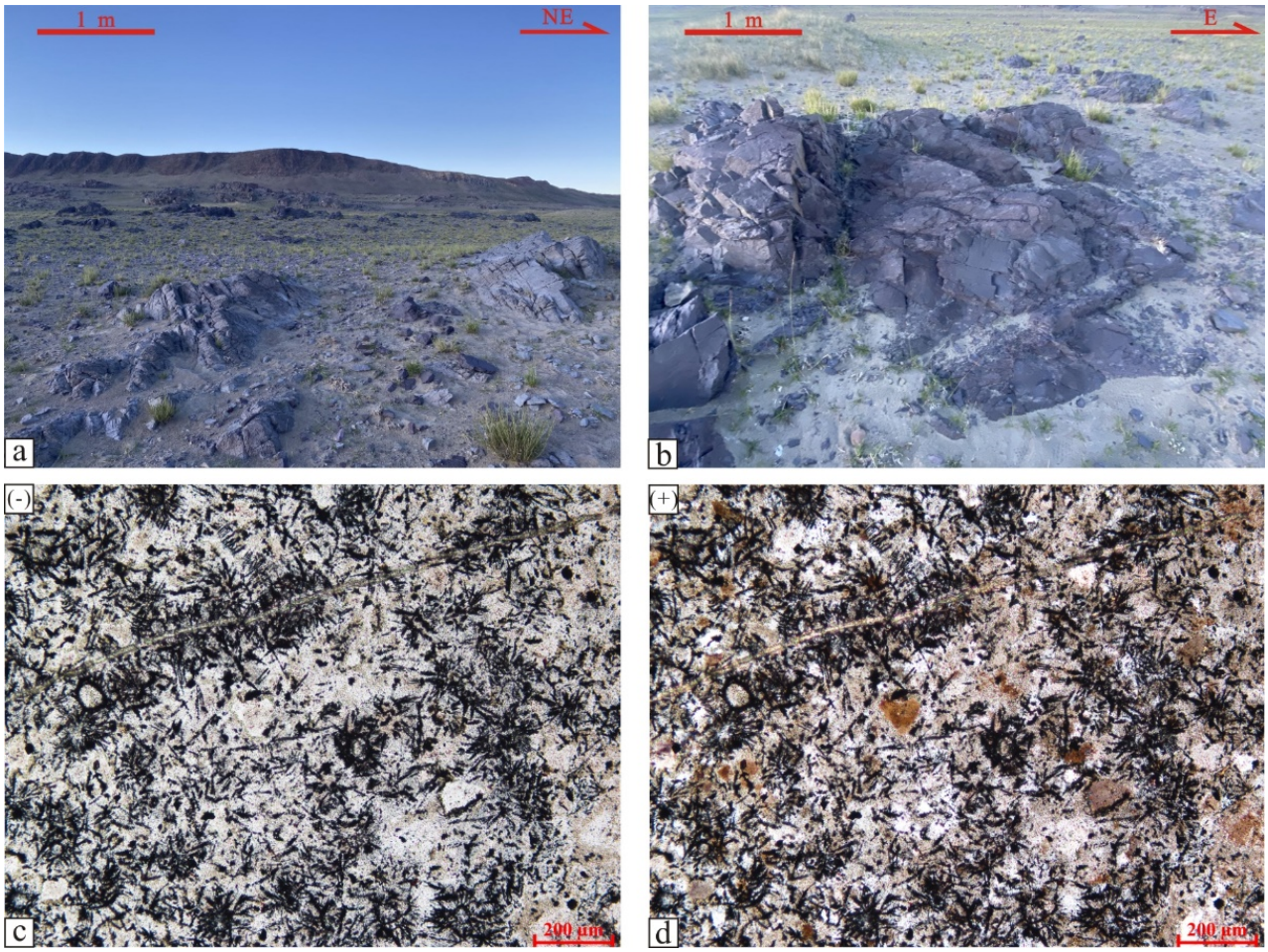

Figure 2. Field outcrops and microscopic mineral photos of volcanic rock in the Jingzhushan Formation from Coqen Basin (**a**–**d**).

The types of debris in the northwest of the county are different from those in the south. The proportion of sedimentary debris increases, and the proportion of sedimentary debris and extrusive debris is the same (Figure 4). Sedimentary debris is composed of mudstone debris and siltstone debris. The mudstone debris is mainly clay minerals, and there is no directional structure. The siltstone debris has a clastic structure, and the size of the debris varies. Basically, it is quartz, and the clay minerals are filled with the quartz. The metamorphic debris is dominated by polycrystalline quartz (Figure 4g,h), and the occurrence frequency is more than that of the southern sampling points, which may represent more tectonic thermal events related to collision orogeny of plates.

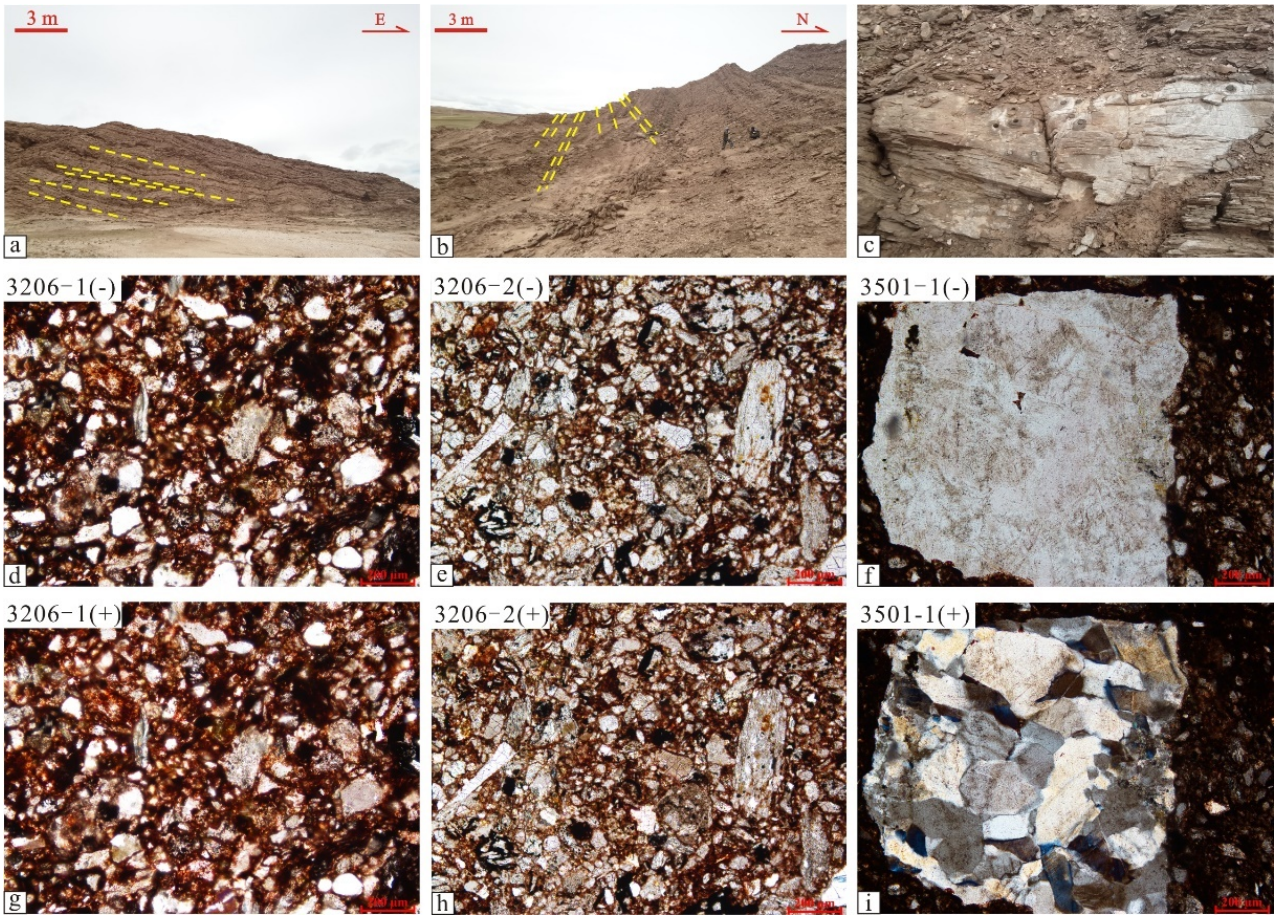

Figure 3. The photo of sandstone minerals and field outcrops in the Jingzhushan Formation on the west side of Nyima County. (**a**,**b**) Occurrence of field profile; (**c**) Outcrops and drilling conditions; (**d**–**f**) Minerals photos under the polarising microscope; (**g**–**i**) Minerals photos under the orthogonal microscope.

Fracture-developed quartz appears in both sampling points, but there are certain differences between the two. On the slice photo of sample 3206 on the west side of the county, most of the quartz grains have micro-fractures developed in different directions, which may be related to sedimentary compaction. However, the slice of KJ0501 sample at the northern sampling point shows that there are also fractures developed, but they are penetrating fractures (Figure 4f). Quartz grains and schist debris or other mineral grains have long fractures in the same direction, indicating that there is only one stage of fracture produced by the compressive orogeny in the Jingzhushan Formation of Late Cretaceous. Such fracture characteristics, which are different from the short fractures produced by sedimentary compaction, can indicate tectonic activity of compressional collision.

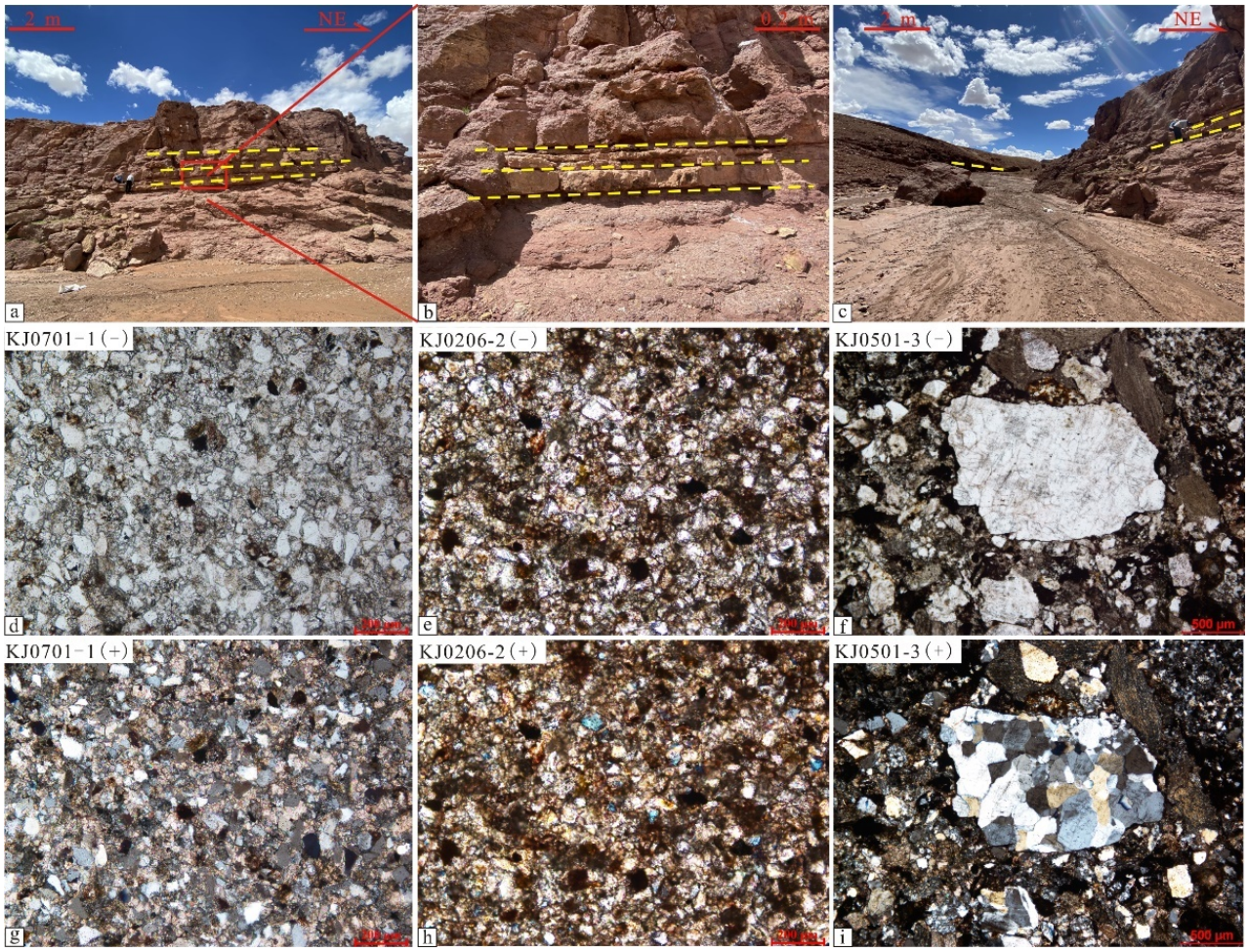

Figure 4. The photo of sandstone minerals and field outcrops in the Jingzhushan Formation on the north side of Nyima County. (**a**–**c**) Occurrence of field profile; (**d**–**f**) Minerals photos under the polarising microscope; (**g**–**i**) Minerals photos under the orthogonal microscope.

4.2. Rock Magnetism

The rock magnetism reflects the types of magnetic minerals contained in the samples through the experiment of saturation isothermal remanence and the curve of systemic thermal demagnetization. The experiment on saturation isothermal remanence (SIRM) utilizes the characteristics of magnetic minerals that tend to saturate with increasing external field, indicating the coercivity of magnetic minerals. The curves of saturation remanence for the sandstone samples in the Jingzhushan Formation from the Nyima Basin (Figure 5a,c) and the eruptive rock samples in the Jingzhushan Formation from the Coqen Basin (Figure 5b) used for zircon dating are consistent.

The intensity of magnetization for the samples did not reach saturation at 2 T, and approached saturation at 2.5 T. The demagnetization rate of the reverse field is slower, both of which indicate that the magnetic minerals in all samples are of high coercivity. The curve of systemic thermal demagnetization shows that the intensity of magnetization for the eruptive rock in the Jingzhushan Formation from the Coqen Basin is the largest (Figure 6); the intensity of magnetization for the sandstone samples from the southern sampling point of the Nyima Basin is higher than that of the northern sampling point. The intensity of magnetization for the two sampling points in the north and south of the Nyima Basin decreased significantly at 675 °C, indicating that the magnetite-bearing minerals are mainly hematite with high coercivity. However, the eruptive rocks of the Jingzhushan Formation from the Coqen Basin have obvious decreasing steps of magnetization intensity at 580 °C

and 675 °C, indicating that magnetite and hematite are deblocked at 580 °C and 675 °C, respectively.

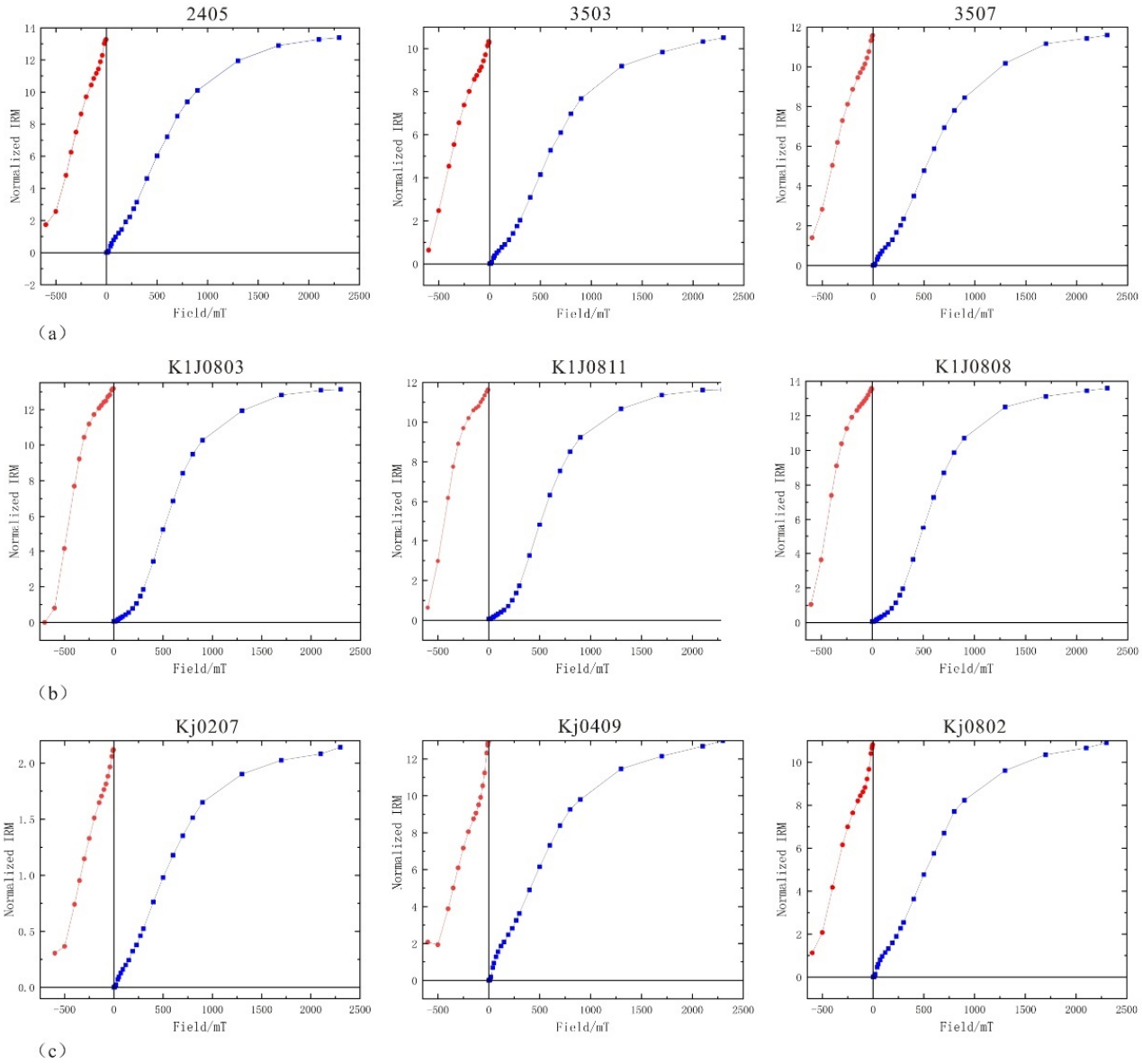

Figure 5. The characteristics of the experimental curve for the saturation isothermal remanence. (**a**) Samples from southern collection site; (**b**) Samples from Coqen Basin; (**c**) Samples from northern collection site. Red dots represent the magnetization in a weakened field; Blue dots represent the magnetization in an enhanced field.

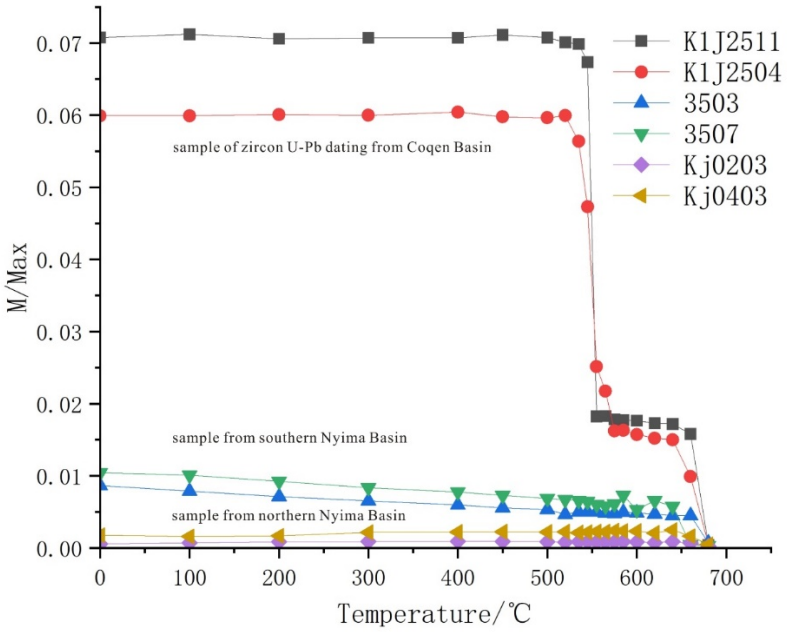

Figure 6. Curve of systemic thermal demagnetization for a typical sample in the Jingzhushan Formation of the Late Cretaceous.

4.3. Scalar Parameters of Magnetic Fabric

The maximum axis (K1), the middle axis (K2) and the minimum axis (K3) of the magnetic susceptibility ellipsoid obtained from the test of magnetic fabric can represent relevant parameters, including the average magnetic susceptibility (Km) [30], anisotropy degree (Pj) [31], shape factor (T) [32], magnetic foliation (F) [33] and magnetic lineation (L). The average magnetic susceptibility (Km) reflects the comprehensive characteristics of the magnetic susceptibility for magnetic minerals, and is related to the type of magnetic minerals [34]. The value of average magnetic susceptibility for the sampling point on the north side is low, with an average value of 155 $\times$ 10^{-6} SI. The values of average magnetic susceptibility at the east and west sampling points in the south side of the county are relatively high, with average value of 194 $\times$ 10^{-6} SI, 234 $\times$ 10^{-6} SI and 372 $\times$ 10^{-6} SI, respectively. On the whole, the range of magnetic susceptibility is (155–372) $\times$ 10^{-6} SI, showing the characteristics of weak magnetic susceptibility. Magnetic lineation (L = K1/K2) shows the degree of linear arrangement for the long axis by sediment particles. Magnetic foliation (F = K2/K3) shows the degree of planar distribution by particle, and the Flinn diagram can reflect whether the sediment particles are in a strained state or a sedimentary state [35]. The Flinn diagram of the sampling point on the north side of the basin (Figure 7a) shows that the samples basically fall in the left area of the line (InF = InL), which belongs to an elongated magnetic susceptibility ellipsoid, and the development of magnetic lineation is stronger than that of magnetic foliation. The Flinn diagram of the sampling point on the south side of the basin (Figure 7b–d) shows that the samples fall in the right area of the line (InF = InL), which belongs to the flattened magnetic susceptibility ellipsoid; and the development of magnetic foliation is stronger than that of magnetic lineation. Combined with the shape factor (T), the values of the northern sampling points are all less than 0, with an average value of -0.463 and a minimum value of -0.759, indicating that the magnetic susceptibility ellipsoid is mainly elongated. The values (T) of sampling points on the south side are all greater than 0, and the magnetic foliation is developed, showing the sedimentary magnetic fabric, and the magnetic susceptibility ellipsoid is flattened.

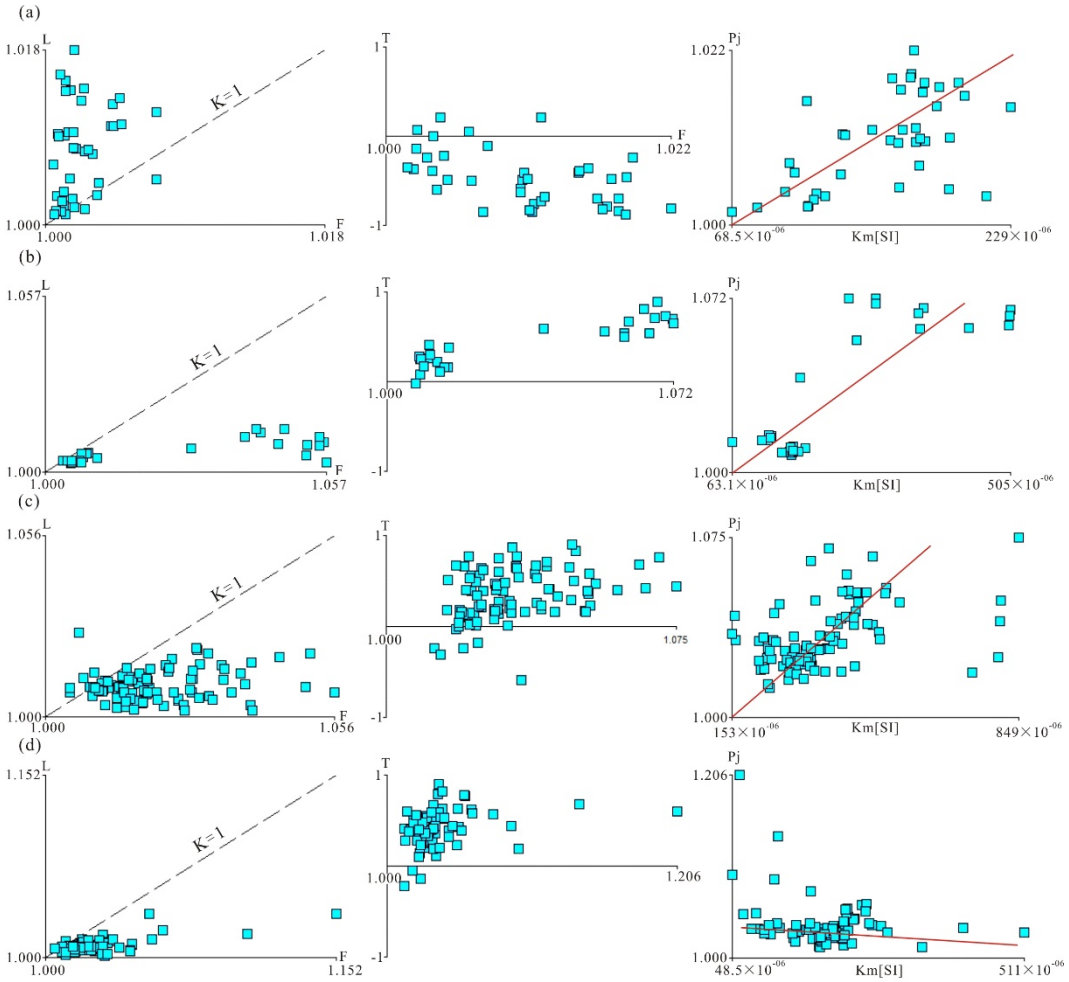

Figure 7. Diagram of magnetic susceptibility parameters for samples from the Jingzhushan Formation in the Late Cretaceous. (**a**) Samples from northwest collection site (KJ 01-08); (**b**) Samples from southwest collection site (KJ24-35); (**c**) Samples from southwest collection site (WKJ01-10); (**d**) Samples from southeast collection site (EKJ01-05). The red line represents a linear correlation.

4.4. Major Axis Orientation of Magnetic Susceptibility Ellipsoid

The corresponding relationship between the major axis of the magnetic susceptibility ellipsoid and that of the strain ellipsoid can reflect the dominant occurrence of rock fabrics [32]. The minimum major axis of magnetic susceptibility (K_{min}) at the southern mining point is basically in the center of the base circle, and there is basically no strain effect, which belongs to the original sedimentary fabric (Figure 8a,b). The K_{max} of the two sampling points is in the second and fourth quadrants and the first and third quadrants, respectively. The distribution of magnetic foliation may represent ancient currents in the NW-SE and NE-SW directions. The distribution of K_{min} at another sampling point is slightly deviated from the center of the base circle, and its K_{max} is distributed in the first, second and fourth quadrants, forming a fan-like distribution, which may represent another form of ancient current (Figure 8c). The magnetic fabric samples at the north side are located near the thrust fault. The stereographic projection of the magnetic susceptibility major axis shows that the maximum major axis of magnetic susceptibility (K_{max}) is mainly distributed in the first and third quadrants, mainly close to the Y axis, showing the dominant direction of NE-SW, which is consistent with the trend of thrust fault. The minimum major axis (K_{min}) is mainly distributed in the second and fourth quadrants, and is preferably close to the X axis. Its dominant direction is the NW-SE direction, indicating that it is subjected to compressive stress in the NW-SE direction (Figure 8d).

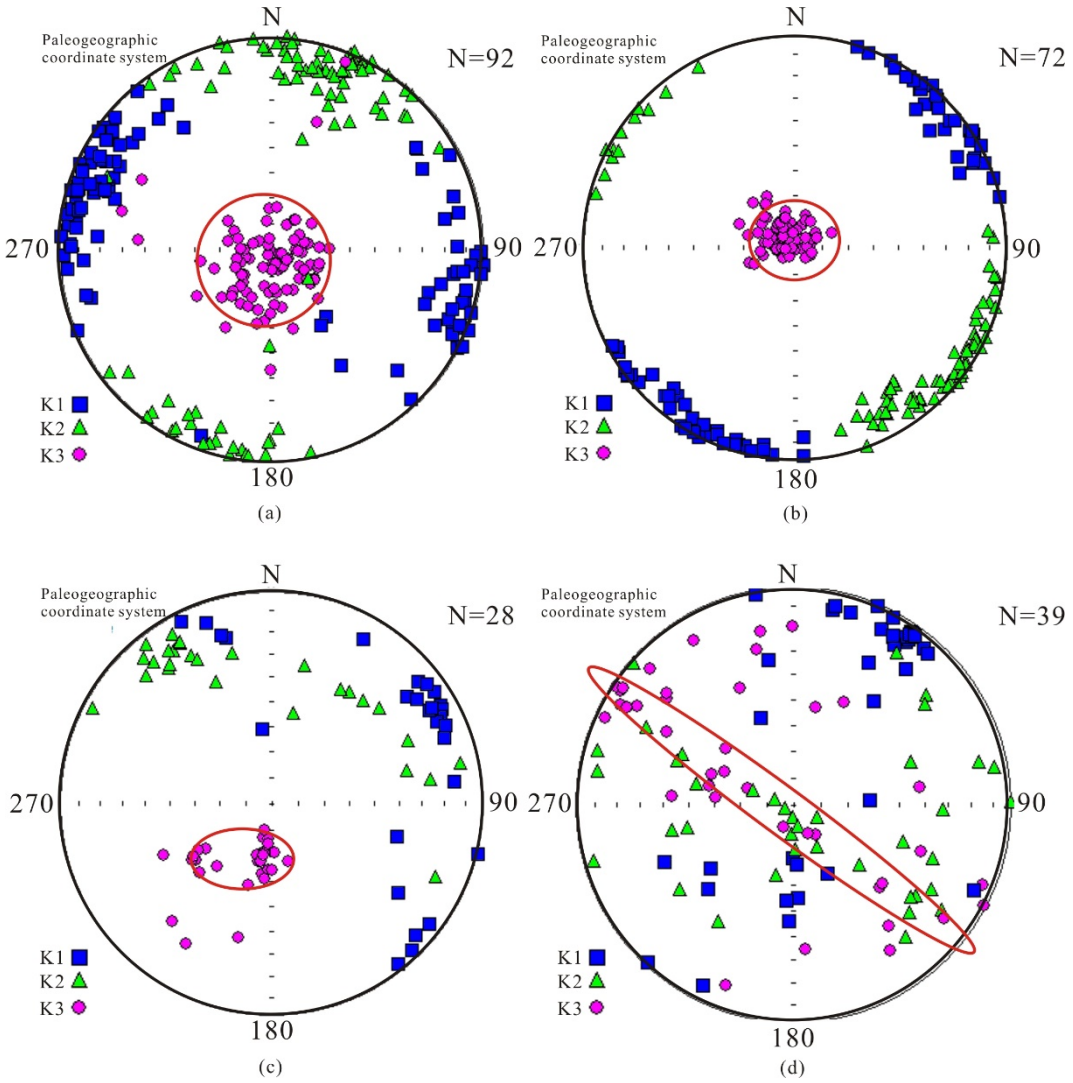

Figure 8. Characteristics of magnetic fabric for the sandstones from different sampling points in the Nyima Basin of Jingzhushan Formaiton in the Late Cretaceous. (**a**) Sedimentary magnetic fabrics indicates NW trending paleocurrent; (**b**) Sedimentary magnetic fabric indicates ES trending paleocurrent; (**c**) Sedimentary magnetic fabric of weak current indicates NE trending paleocurrent; (**d**) Strain magnetic fabric. Red circle represents the direction of extrusion stress.

4.5. Zircon Geochronology

Existing chronological studies of the Jingzhushan Formation focus on the red bed of clastic rocks. For this reason, we specially selected the purple-red extrusive rocks of the Jingzhushan Formation in the Coqen Basin to carry out zircon U-Pb dating, in order to study the age difference and compare provenance. The zircon particles in extrusive rock samples have both columnar and irregular shapes with a low degree of abrasion, and elliptical shapes with high roundness. This indicates the presence of both distant and near-source transport. Most of the grains have oscillating rings of magmatic origin, and a few may appear as white and without clear rings due to lack of U/Th (Figure 9a). Thirty-one effective ages were obtained from the 35 measuring points of the sample, and the main ages were concentrated at 92–124.6 Ma and 182–461 Ma. There are also individual measuring points whose ages are 1150 Ma, 1414 Ma, 2150 Ma and 2650 Ma. The 92 Ma age represents the youngest eruption age of the Jingzhushan Formation (Figure 9b,c). In addition, we refer to the zircon age of the Jingzhushan Formation in the Geji area of the northern Lhasa Block [36]. This age is highly similar to the age of the eruptive rocks in the

Coqen Basin in the range of 0–300 Ma. From its peak age, it can be seen that the volcanic eruption time of the northern Lhasa Block is around 110 Ma and 160 Ma (Figure 9d,e).

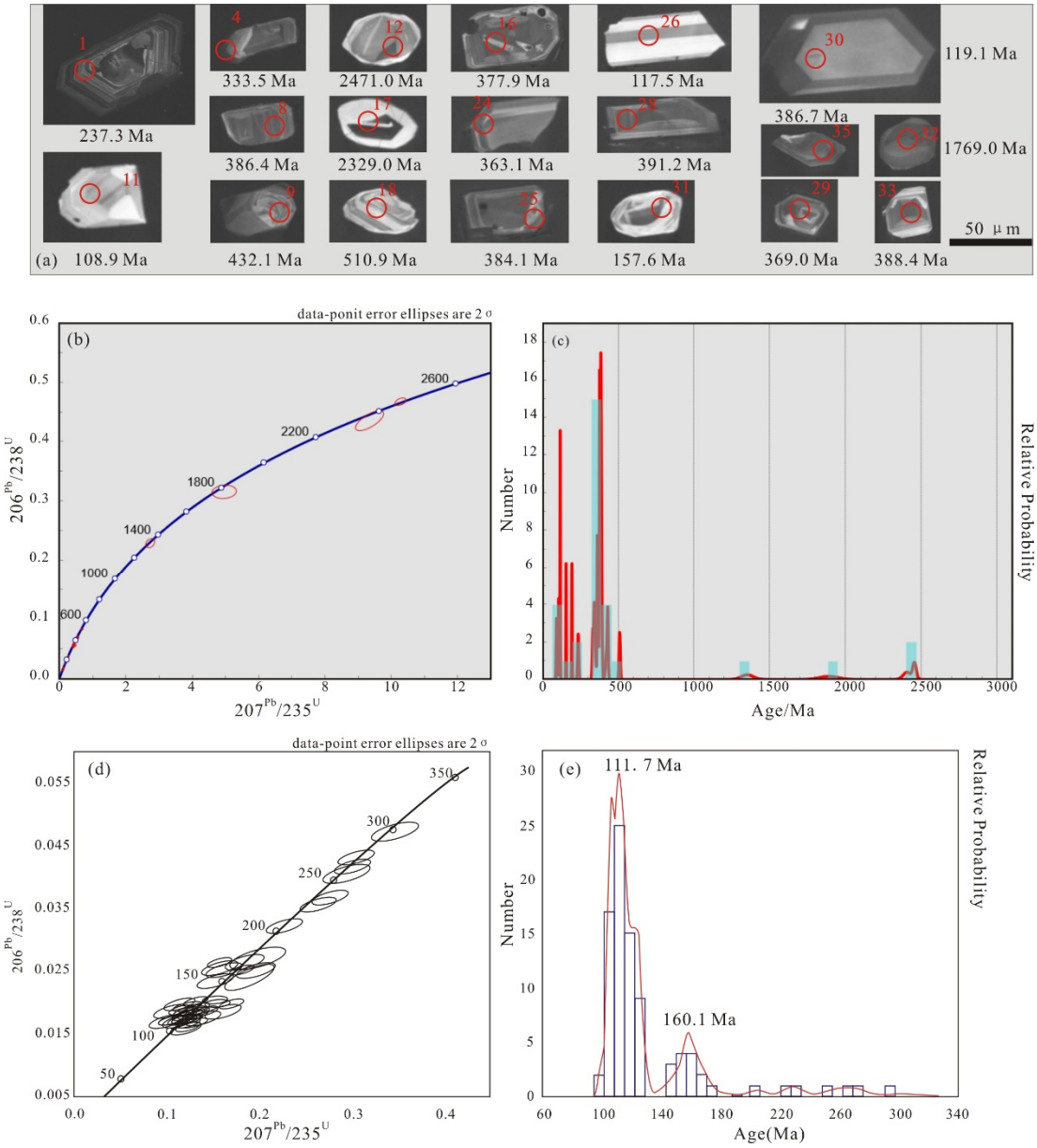

Figure 9. Zircon morphology and age spectrum of the volcanic eruptive rocks in the Jingzhushan Formation of Late Cretaceous from the Coqen Basin and the zircon age quoted in the Geji area [36]. (**a**) zircon morphology of eruptive rock; (**b**) harmonious ages of eruptive rock; (**c**) age spectrum of eruptive rock; (**d**) harmonious age of detrital zircon from Geji area; (**e**) age spectrum of detrital zircon in Geji area. Red and black circles represent the age aggregate region.

5. Discussion

5.1. Differences in Magnetic Minerals

The average value of magnetic susceptibility for the red-bed samples in the Jingzhushan Formation from the Nyima Basin is between 104 × 10^{-6} SI and 542 × 10^{-6} SI. Tarling and Hrouda (1993), believed that the magnetic minerals in the samples whose average value of magnetic susceptibility was less than 5 × 10^{-4} SI were mainly paramagnetic minerals [32], so it can be considered that most of the magnetic minerals in the red-bed samples were paramagnetic minerals. Referring to the average magnetic susceptibility (Km), anisotropy

(Pj) and shape factor (T) of common magnetic minerals (Table 2), the magnetic minerals at the northern sampling point are multidomain magnetite [37,38] and the magnetic minerals at the south side are hematite and a small amount of magnetite [39,40]. The values (Km) of the samples in the basin are basically divided into three groups, namely (100–200) $\times$ 10^{-6} SI, (200–400) $\times$ 10^{-6} SI and (400–600) $\times$ 10^{-6} SI. The observation of rock slices shows that the main mineral in the red layer of the Jingzhushan Formation is quartz, including a very small amount of feldspar, white mica, biotite, magnetite, sericite and chlorite. The mineral composition of the northern sample with value (Km) of (100–200) $\times$ 10^{-6} SI should be quartz [41,42], chlorite and sericite. The mineral composition of the southern samples with values (Km) of (200–400) $\times$ 10^{-6} SI and (400–600) $\times$ 10^{-6} SI should be quartz, biotite, white mica and chlorite.

The difference in the average magnetic susceptibility between the north and south sampling sites may be caused by the difference in the quantity of paramagnetic and diamagnetic minerals. Quartz grains in the northern sampling point are large and numerous, and sericite with directional structure exists, resulting in a lower value (Km) overall. The number of paramagnetic minerals in the sampling point on the south side is large, mainly biotite, white mica and chlorite, while the number of quartz particles belonging to diamagnetic mineral is relatively small and the particle is small. This indicates that the value (Km) of the red layer in the Jingzhushan Formation is basically less than 500 $\times$ 10^{-6} SI, which is controlled by paramagnetic mica minerals, and the minerals with value (Km) greater than 500 $\times$ 10^{-6} SI may be joined by ferromagnetic minerals [32,38,43,44]. At the same time, the study of rock magnetism shows that the intensity of magnetization for the samples from the southern sampling site is greater than that of the northern sampling site. Although the magnetic minerals are all high-coercivity magnetite, the systemic thermal demagnetization shows that the magnetic minerals in the northern samples are only magnetite, while the magnetic minerals in the southern samples are magnetite and hematite.

Table 2. Reference values of average magnetic susceptibility (Km), anisotropy (Pj) and shape factor (T) for common magnetic minerals [45].

Magnetic Mineral	Average Volume Susceptibility (SI) $\times$ 10^{-6}	Pj	Average Value (Pj)	Average Value (T)	References
Ferromagnetic mineral					
magnetite (αFe_3O_4) MD	<3000	1.1~3.0	1.18	−0.3	[35]
magnetite (αFe_3O_4) SD	<1500	∞	-	-	[37]
magnetite (αFe_3O_4) SP	<5000	…	-	-	[37]
hematite (αFe_2O_3)	~1300	>100	-	~1.0	[32]
maghemite (γFe_2O_3)	~2500	500	-	+	[32]
pyrrhotite (Fe_7S_8)	~1000–10^6 SI	3~400	0.8	+	[39]
goethite (αFeOOH)	~1000	+	-	+	[39]
Paramagnetic mineral					
white mica	~150	-	1.15	0.84	[21]
biotite	~1250	1.12~1.6	1.31	0.96	[21]
chlorite	~300–1500	1.2~1.7	1.15	0.95	[21]
chloritoied		1.47 ± 0.06	1.47(HF)	0.9(HF)	[21]
amphiboles	746–1368	-	-		[21]
siderite	470	-	-		[43]
pyrite	35~5000	-	-		[38]
Diamagnetic mineral					
quartz	−13.4~−15.4	-	1.01	1.00	[38]
feldspar	−13~−17	-	-	-	[21]
calcite	−12.82	1.13	1.11	1.00	[37]
dolomite	−6.24	-	-	-	[32]

5.2. The Reason for the Formation of the Magnetic Fabric

The features of magnetic fabric are represented by the three axes (K1, K2, K3) of the magnetic susceptibility ellipsoid. In the study of the Eocene mudstone in the southern Pyrenees, Pares et al. (1999) proposed three evolutionary stages of the magnetic fabric, including the initial deformation fabric, the pencil-like fabric and the weak cleavage fabric [24]. In the study on the Longmen Mountain fault zone, Jia et al. identified 6 types of magnetic fabrics, including the strong cleavage and tensile lineation fabrics with stronger deformation [46]. The magnetic fabrics studied here are more in line with sedimentary fabric, pencil-like fabric and tensile lineation fabric in terms of the distribution characteristics of the K_{max} and K_{min}. Therefore, the magnetic fabric features of the four sampling points correspond to two types of sedimentary fabric and strain fabric (Figure 10). Sedimentary fabrics include a hydrostatic environment and weak current environment, and strain fabrics include pencil-like fabric and tensile lineation fabric.

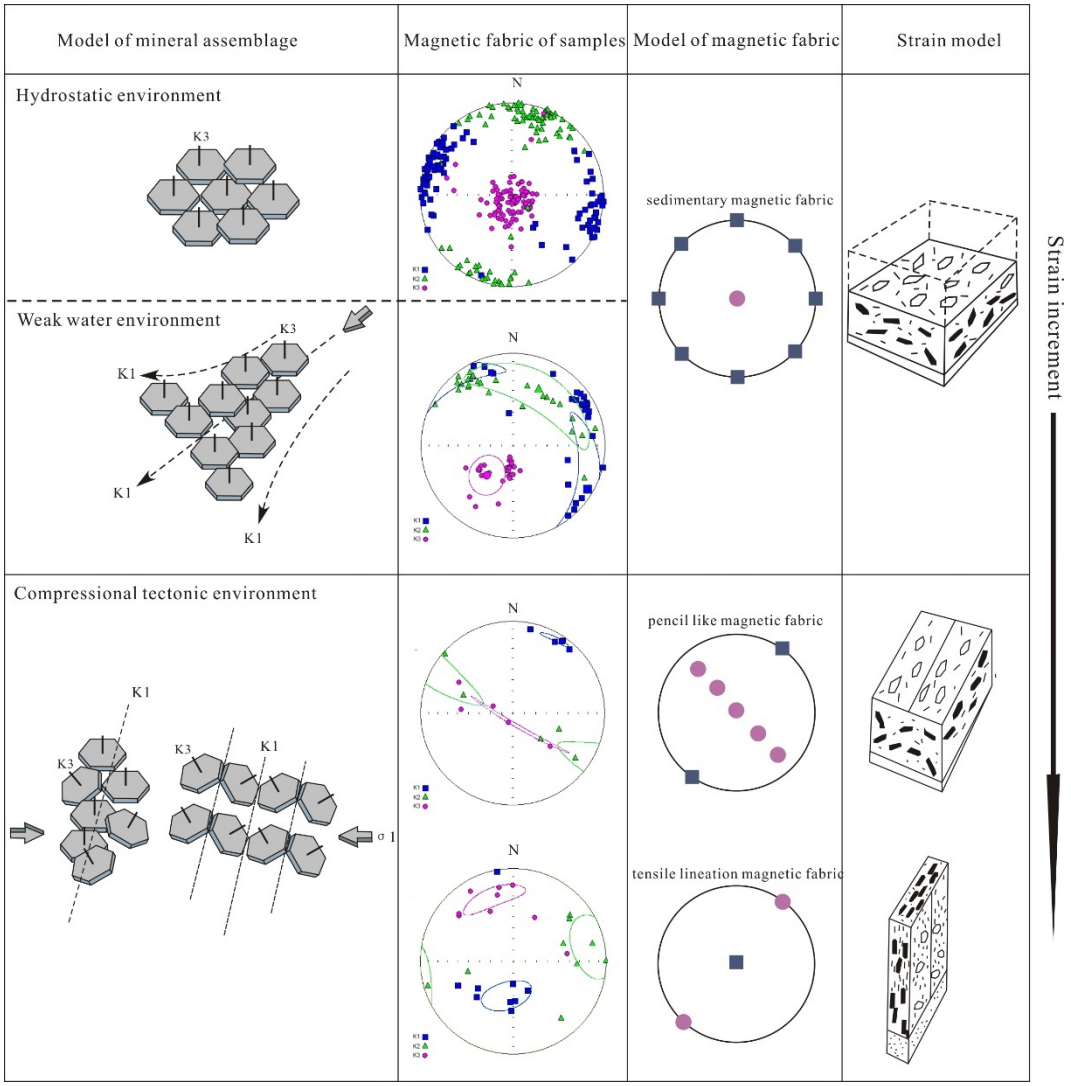

Figure 10. Different features of magnetic fabrics and corresponding modes of formation.

For the sedimentary magnetic fabric, in a relatively hydrostatic environment where layered silicate minerals are deposited parallel to the layers, K_{min} is perpendicular to the layers, while K_{max} is orientation reflects the random arrangement of minerals. In a weak current environment, driven by hydrodynamic forces, the silicate minerals will be arranged in imbricates, showing that K_{min} slightly deviates from the center of the base circle, while

K_{max} is predominant in a fan-shaped distribution [47]. The dominant direction of the K_{max} in the magnetic susceptibility ellipsoid of the two sedimentary fabrics may represent the direction of the paleocurrent. In the strained magnetic susceptibility ellipsoid, whether it is a pencil-like fabric or a tensile lineation fabric, the K_{min} is distributed in NW-SE, indicating that there is extrusion in the NW-SE direction. The K_{max} is perpendicular to K_{min} and is distributed in the NE-SW direction, which is consistent with a stratigraphic strike and also reflects its formation in a compressional environment (Figure 10) [48].

5.3. Sedimenatary Magnetic Fabrics Correspond to Paleocurrents

The sedimentary fabrics of the Nyima Basin have two magnetic lineations (K1) in the dominant directions. Since two directions of magnetic lineation are generated in the Jingzhushan Formation, it is less likely to reflect plate rotation during a such relatively short depositional period, so the directions of magnetic lineation may reflect the ancient currents in NW-SE and NE-SW directions. There are few studies on the paleocurrent of the Jingzhushan Formation in the Nyima Basin. Decelles et al. (2009) believed that there were multiple changes of paleocurrent in the Cretaceous of the Nyima Basin [29]. The direction of paleocurrent reflected by sedimentary fabric is shown in Figure 11. The formation of the bidirectional paleocurrent is related to the paleogeomorphology influenced by thrust structures. The uplift of the hanging wall of the reverse fault caused the topography on both sides to decrease, forming a bidirectional paleocurrent. The formation of unidirectional paleocurrent may be that the water source was located at a relatively low point in the hanging wall, so it could only flow to one side. As the strata denudation intensified, the low point gradually turned into a high point and began to flow to both sides. Therefore, the unidirectional paleocurrent reflected by the sedimentary fabric should be the initial state when the hanging wall had not been denuded.

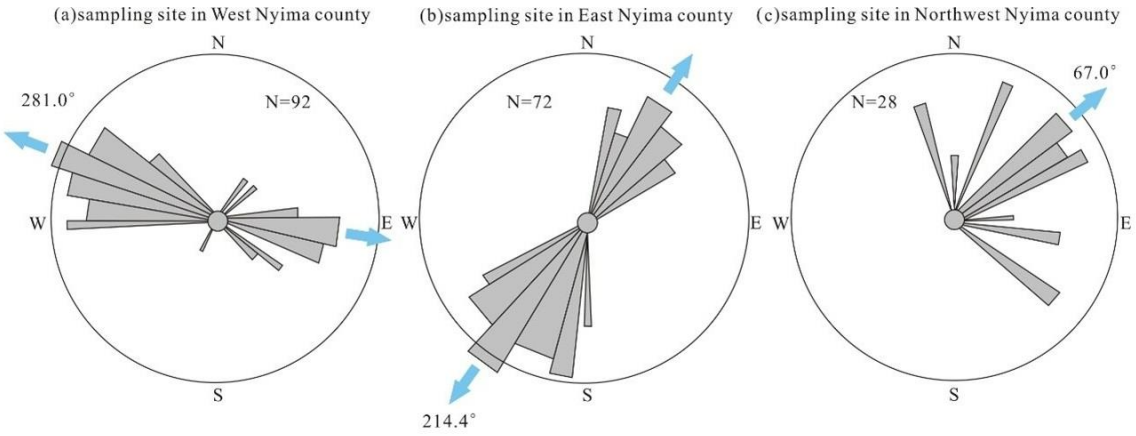

Figure 11. Paleocurrent in rose diagram at different sampling points in the Nyima Basin.

5.4. Interpretation of Magnetic Fabric for Thrust Structure

The extrusion direction represented by the minimum axis (K3) of the magnetic susceptibility ellipsoid of the pencil-like fabric and tensile lineation fabric is in a NW-SE direction, 298.4° (Figure 12d). The strong strain magnetic fabric exhibited by the minerals can explain the widely developed thrust structures in the basin. Two different strains can be generated by the tectonic deformation process, namely the parallel layer shortening (LPS) before folding [49] and the strain during folding. Sedimentary fabric, initial deformation fabric and pencil-like fabric represent the results of LPS [50]. The weak cleavage fabric, strong cleavage fabric and tensile lineation fabric are more likely to occur in the process of folding. In addition, the small-angle oblique stratum of magnetic foliation is different from the strain fabric in this study, so it does not belong to the magnetic fabric generated by the LPS process [51]. The magnetic foliation of the strained fabric is oblique to the stratigraphic layers at a large angle (Figure 12d), and the tensile lineation fabric and the pencil-like fabric

develop strongly at the roots of the thrust structures. The above shows that the strained magnetic fabric belongs to the limited strain fabric with single shear properties in the process of folding.

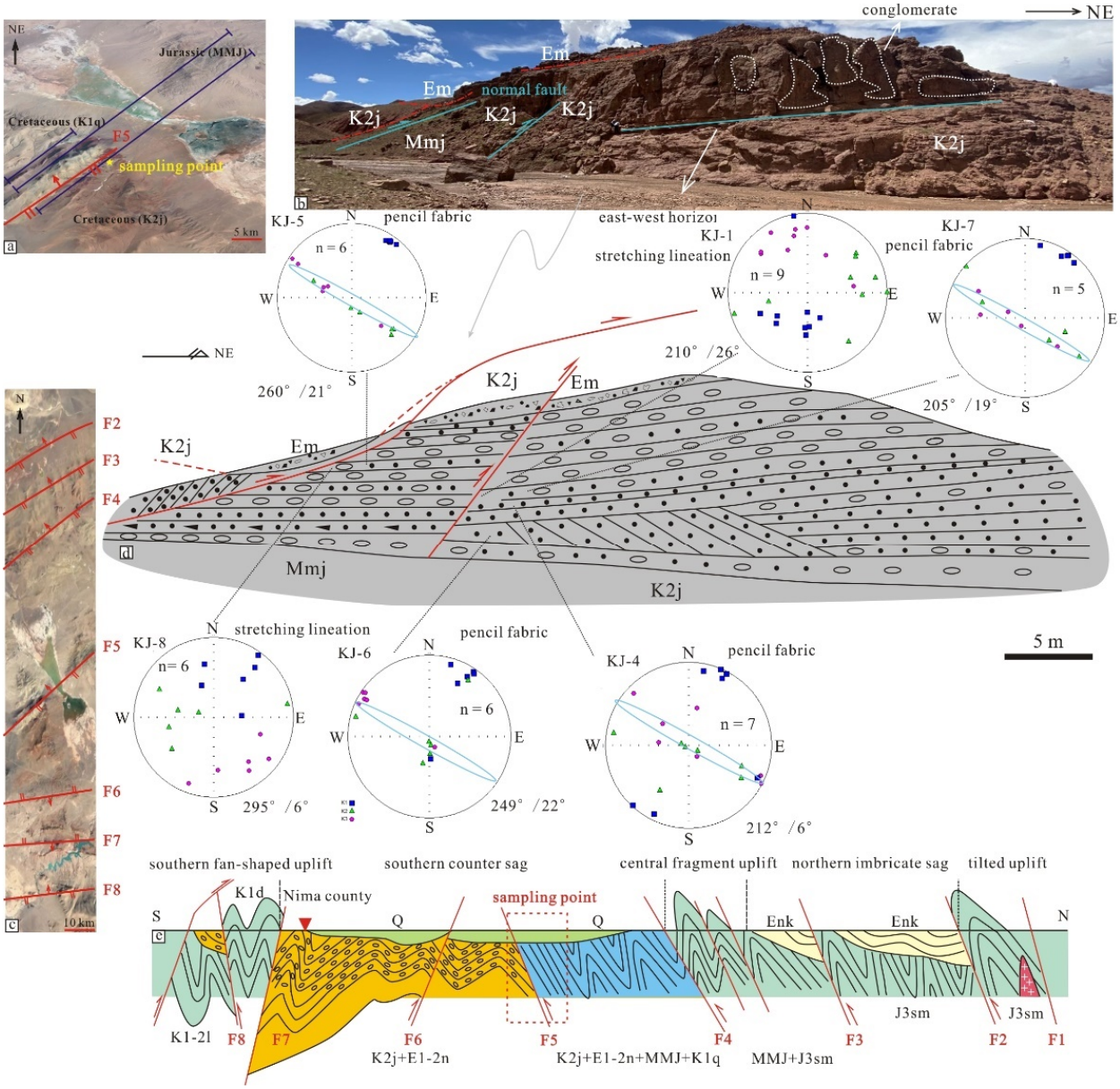

Figure 12. Magnetic fabric characteristics of thrust structures in the Nyima Basin. (**a**) trend of thrust fracture where the strain fabric is located; (**b**) the fracture section where the strain fabric is located; (**c**) distribution of main faults in Nyima Basin; (**d**) the relationship between lithology, formation contact and strain fabric of the fault section where the strain fabric is located; (**e**) the north-south transverse section of the main fault in the Nyima Basin.

Magnetic susceptibility ellipsoids in deformed rocks have a good correspondence with strain ellipsoids [21,52]. The predominant direction of the minimum axis in the magnetic susceptibility ellipsoid corresponds to the direction of the maximum compressive stress [32]. This vector of compressive stress is defined as R and the corresponding components N and P are decomposed along the horizontal and vertical direction of the fracture surface. Combined with the fault strike of the horizontal plane and the fracture tendency of the transverse section, the kinematics analysis was carried out [51]. In the six sampling points near the fracture where the strained magnetic fabric is located, the major axis of the

minimum magnetic susceptibility is in the NW-SE direction, and the spatial direction of dominant vector is 298° ∠26°, reflecting the extrusion in this direction. On the plane, it is oblique to the fault strike. Therefore, the vector represented by the major axis of the minimum magnetic susceptibility is decomposed along the fault strike and perpendicular to the fault strike direction. The decomposition results show that there is a clockwise component, indicating that the fracture trend twists clockwise on the plane (Figure 13). This indicates that the fracture has motion features of the right strike-slip in the horizontal motion. In vertical cross-section, the major axis of minimum susceptibility is oblique to the fracture tendency. The vector represented by the minimum magnetic susceptibility is decomposed along the fault inclination line and its vertical direction, and the results show that there is a vertical rotation in a clockwise direction, indicating that the SW disk is rising relative to the NE disk, and the fault has a thrusting property (Figure 13). The above shows that the fracture where the strain fabric is located is dominated by a SW trending thrust under the extrusion in NW-SE direction, accompanied by a certain right strike-slip.

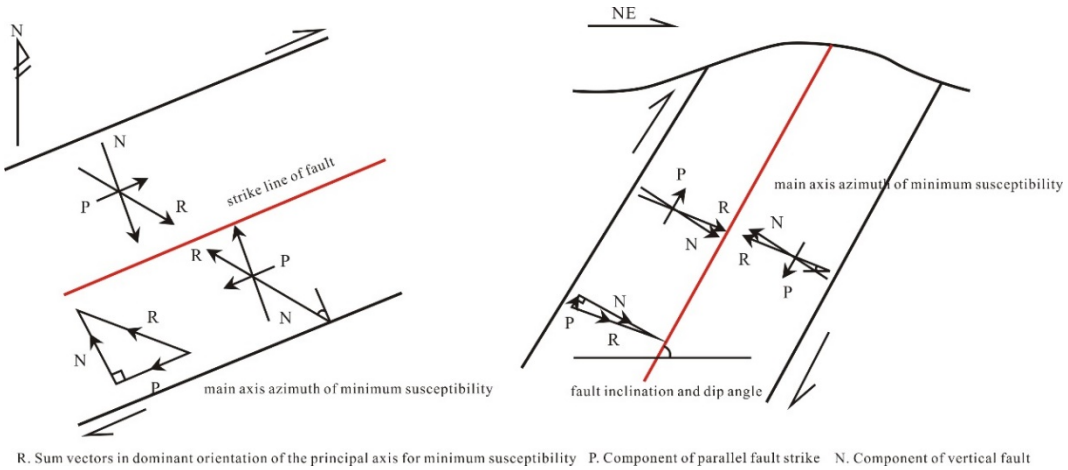

Figure 13. Analysis of the motion relationship between magnetic fabric and thrust fault.

Since the thrust faults in the Nyima Basin have two thrust directions, from south to north and from north to south, the regional thrust structures in hedging type formed in this basin shows that the Nyima Basin is simultaneously subjected to drag forces by plate subduction from two directions (Figure 14). The plate subduction from north to south is caused by the Bangong-Nujiang Oceanic Basin. The re-subduction to the south may indicate that although the Bangong-Nujiang Oceanic Basin was subducted northward to combine with the South Qiangtang Block during the Late Jurassic to Early Cretaceous, there was still a residual oceanic basin that was subducted southward again in the Jingzhushan Formation. In addition, the plate subduction from south to north is caused by the Namtso-Shiquan River small oceanic basin. The southward subduction of the Bangong-Nujiang Ocean and the northward subduction of the Yarlung-Zangbo Tethys Ocean led into the subduction of the Namtso-Shiquan River small oceanic basin to the Central Lhasa Blcok during the Early Cretaceous [53]. The Zenong Group volcanic rocks from Early Cretaceous in the southwest of Namtso are the products of this subduction. In addition, diabase bodies (133–114 Ma) from early Cretaceous in the Yongzhu ophiolite are found on the west shore of Namtso, indicating that the Namtso small oceanic basin remained open in the Early Cretaceous until the Late Cretaceous [54].

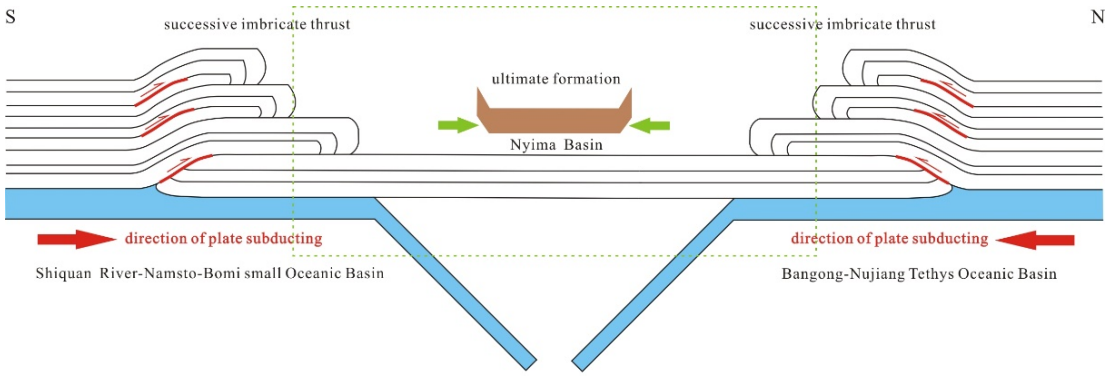

Figure 14. Formation mechanism of thrust structure in hedging type in the Nyima Basin.

5.5. Provenance Analysis

Provenance analysis of the sedimentary systems by detrital zircon is based on the high stability of zircon [55] and characteristics of the sedimentary cycle. By studying the spectrum of detrital zircon, information such as sedimentary sources and evolution of tectonic-thermal events can be obtained [56]. According to the statistics of the age spectrum of zircon age for the Shigatse fore-arc basin, the central Lhasa Block, the north Lhasa Block, the Bangong-Nujiang Suture Zone and the south Qiangtang Block, the Cretaceous strata mainly include 90 Ma, 113 Ma and 125 Ma zircons (Figure 15), which correspond to the Cretaceous magmatic events in the Lhasa Block [57–59]. It has a high coincidence in age peaks after 113Ma during the period of Jingzhushan Formation, when deposited in the Nyima Basin, North Lhasa Block and the same period in the South Qiangtang Block named Abushan Formation. The geological events after 113Ma must correspond to plate collision and continental orogeny. At the same time, it shows that the Jingzhushan Formation in the North Lhasa Block is homologous to the Abushan Formation in the South Qiangtang Block, and the common provenance area of two should be the Bangong-Nujiang orogenic belt (Figure 15a). It was subjected to severe denudation and received sediments to the north and south sides, respectively. On the whole, the high coincidence of the age spectrum represents the experience of a common magmatic event. The age of detrital zircon for 1800–2000 Ma represents the formation of the Gondwana Continent super-basement [5]. The difference between the peak age of the Lhasa Block at 1100 Ma and the peak age of the Qiangtang Block at 950Ma indicates that the Lhasa Block is related to the Gondwana continent, Australia [55,59]; 800 Ma represents the late Jinning Movement [42,60]; 500 Ma records the widespread Pan-African movement in Gondwanan Continents; 400 Ma is associated with thermal events triggered by the subduction closure of the Paleo-Tethys Ocean.

The age of 160–200 Ma is mainly in the South and North Lhasa Block, corresponding to the arc magma generated by the early subduction of the Tethys Ocean. The age of 150 Ma is shared by the South Qiangtang Block and the North Lhasa Block, which is related to the subduction of the Bangong-Nujiang Oceanic Basin and the South Qiangtang Block. The age of 90–120 Ma represents the magmatic events for subduction between the Bangong Co-Nujiang Tethys Ocean and the Yarlung-Zangbo Tethys Ocean. The age of 90 Ma and later appear in the South Qiangtang Block and the northern margin of Lhasa Block, which would indicate the collision orogeny of the Jingzhushan Formation in the Late Cretaceous. Comparing the zircon ages of the Jingzhushan Formation and the Abushan Formation of the Lhasa Block and the South Qiangtang Block in the same period of the the Late Cretaceous, the age spectra of the two blocks are highly similar after 1000 Ma. The age consistency of the southern Nyima Basin, Duoba area and Asuo area is higher, indicating that there is a provenance exchange in these three areas (Figure 15). The North Lhasa Block and the South Qiangtang Block have higher age consistency, indicating that there is also a provenance exchange between the two. To sum up, the provenance area of the Nyima Basin includes both the Lhasa Block and the South Qiangtang Block.

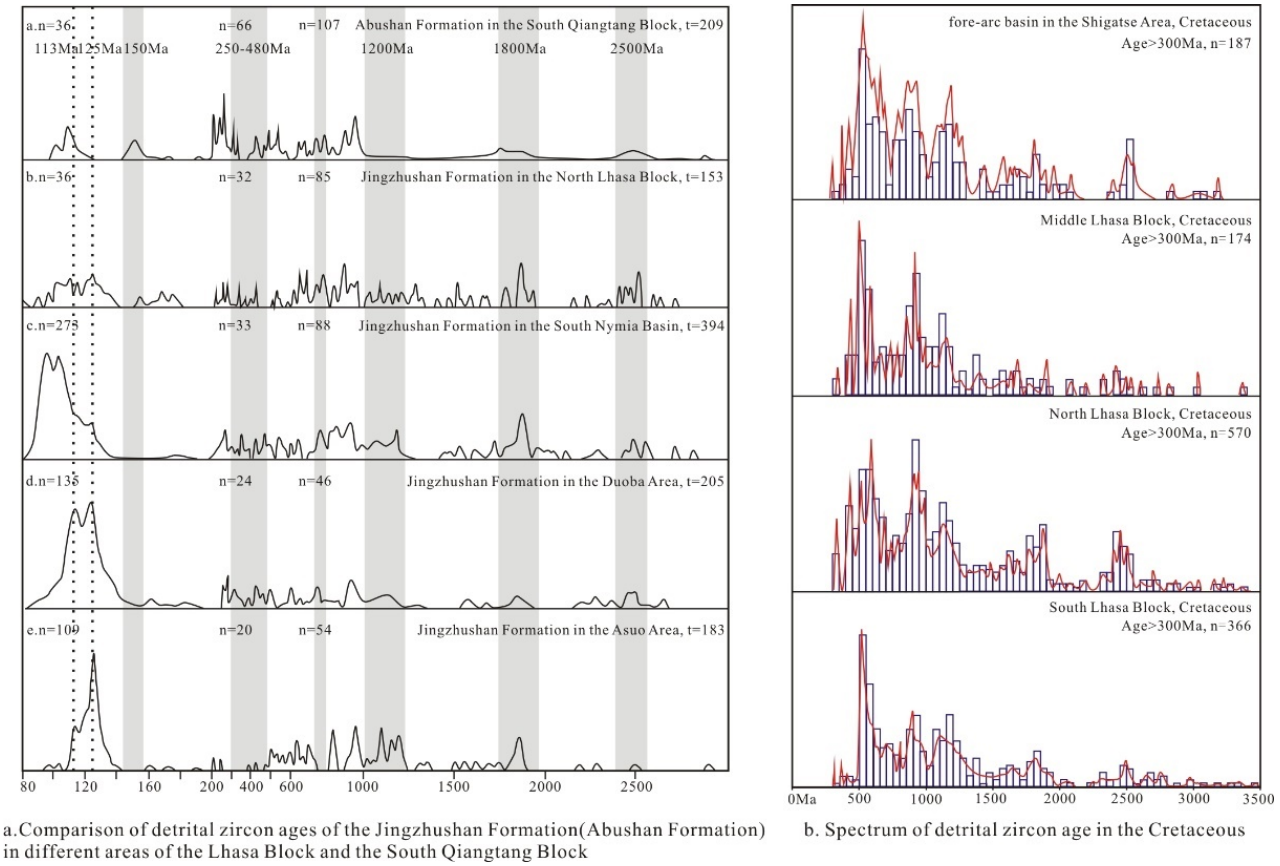

Figure 15. Age spectra of detrital zircon age in the Jingzhushan Formation and Cretaceous [61].

5.6. Tectonic Properties and Evolutionary Process of the Nyima Basin

Dickinson diagrams show that the red-bed samples of the Jingzhushan Formation in the Nyima Basin mainly fall into the environment of a magmatic island arc (Figure 16), which indicates that the tectonic environment is dominated by magmatic island arcs on the active continental margin, and has been denuded for a long time, rather than subjected to the tectonic background of the cyclic orogenic belt. Combined with the hedging thrust structure developed in the basin, it is believed that the soft collision mechanism of "arc-arc (continent)" is more suitable for the formation mode of the Nyima Basin, rather than the rifted basin under the background of "continental-continental" collision in the traditional sense. Moreover, the molasse type also belongs to the ocean-continent transition. In this regard, the tectonic properties of the Nyima Basin should be soft collision for "superimposed zone" between the magma arc generated by the northward subduction of the Namtso-Shiquan River small oceanic basin and the magma arc generated by the southward subduction of the Bangong-Nujiang residual oceanic basin. The sedimentary front area of the Bangong-Nujiang Tethys Ocean is formed under the denudation. At the same time, there is much metamorphic clastic debris in the mineral slices, such as quartz debris under recrystallization (Figures 3f,i and 4f,i) or schist debris. This also indicates that the sandstone minerals of Jingzhushan Formation are mostly derived from arc magmatic rocks.

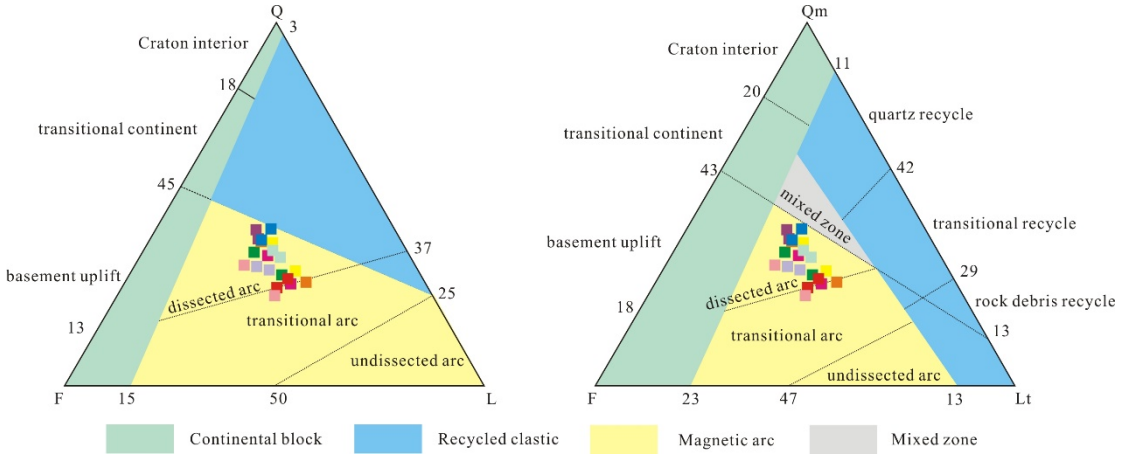

Figure 16. Analysis of tectonic background based on Q-F-L and Qm-F-Lt [55].

The specific process of tectonic evolution is proposed as follows (Figure 17): a. During the Early and Middle Jurassic, the Yarlung-Zangbo Tethys Ocean subducted northward, and the Bangong-Nujiang Tethys Ocean subducted southward. Along with continuous subduction, arc basin systems (fore-arc basins, island arcs, and back-arc basins) were formed on the margins of the central and northern Lhasa Block. The mid-oceanic ridge of the Namtso-Shiquan River Ocean spread and developed between the Middle Lhasa Block and the North Lhasa Block [14,62]. b. From the Middle Jurassic to the Early Cretaceous, the Yarlung-Zangbo Tethys Ocean and the Bangong-Nujiang Tethys Ocean floors continued to be subducted in their original direction. However, the Namtso-Shiquan River small oceanic basin began to subduct southward, forming an arc-basin systems on the northern margin of the Central Lhasa Block. The subduction polarity of the Bangong-Nujiang Oceanic Basin changed, from southward to northward subduction gradually, and the oceanic basin also began to decrease. The subducting polarity of the Namtso-Shiquan River small oceanic basin also changed, from southward subduction to northward subduction, forming an arc-basin system on the southern margin of the North Lhasa Block. c. By the Late Cretaceous, the Yarlung-Zangbo Tethys Ocean continued to be subducted northward, the area of the Namtso small oceanic basin decreased, and the residual oceanic basin continued to subduct northward. At this time, the subducting polarity of the remnant Bangong-Nujiang Oceanic Basin changed again and became a southward subduction. Finally, only the Yarlung-Zangbo Tethys Ocean was still subducting northward, and the plates of the Bangong-Nujiang Oceanic Basin and the Namtso small oceanic basin were fragmented and stopped subducting. The Bangong-Nujiang Tethys Ocean and the Namtso-Shiquan River Ocean became completely closed, forming the Bangong-Nujiang Suture zone and the Shiquan River-Namtso-Bomi Suture zone, respectively. In this way, the integration between the North Lhasa Block and the Central Lhasa Block, and that between the Lhasa Block and the South Qiangtang Block was fully realized. As a foreland basin, Nyima Basin was formed under the combined action of the southward subduction by the Bangong-Nujiang Oceanic Basin and the northward subduction by the Namtso-Shiquan River small oceanic basin, and developed a thrust structure. As a result, the Nyima Basin was formed under the combined action of the southward subduction by the Bangong-Nujiang Oceanic Basin and the northward subduction by the Shiquan River-Namtso small oceanic basin. This was actually the "soft collision" of the arc-basin system by the North Lhasa Block and the South Qiangtang Block. As a foreland basin, thrust structure developed during the orogenic process.

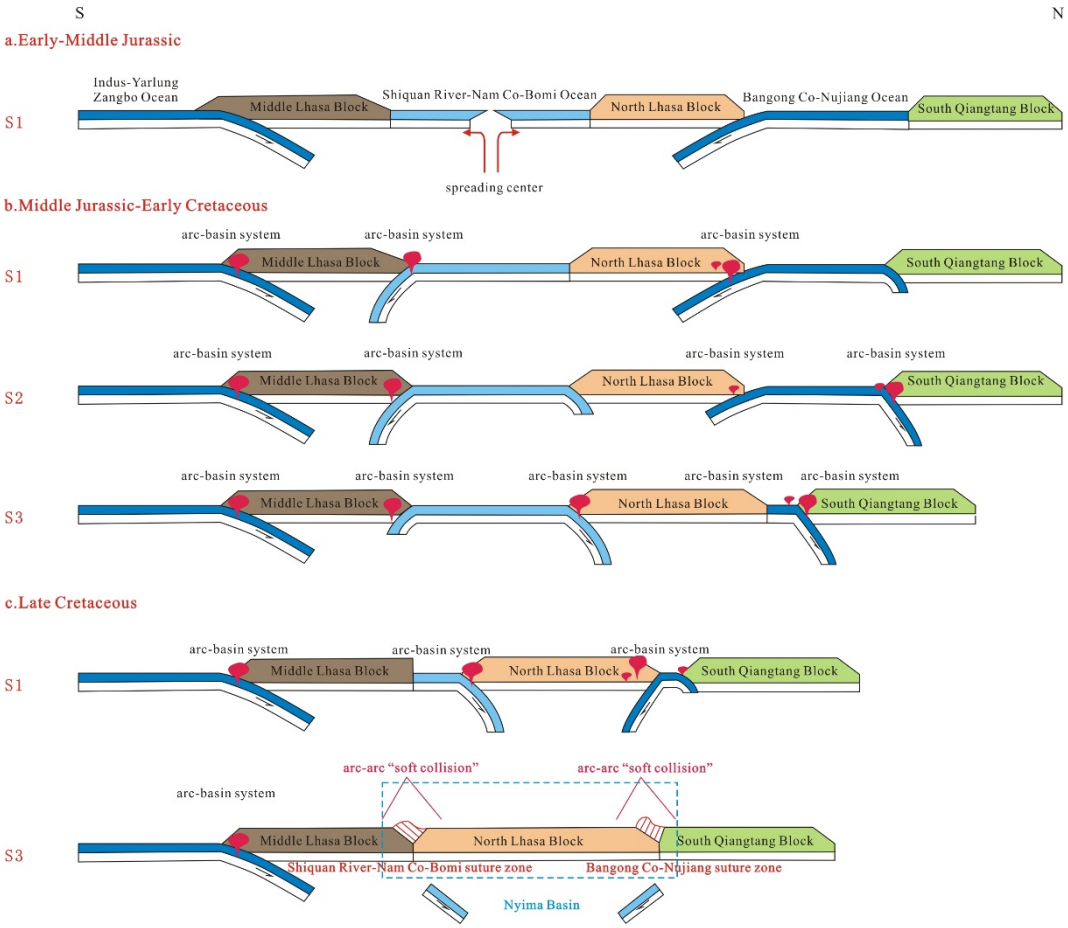

Figure 17. Formation and tectonic evolution of the Nyima Basin during the Early Jurassic to the Late Cretaceous.

6. Conclusions

Studies of mineral magnetic were carried out on the red beds of the Jingzhushan Formation in the Late Cretaceous from the Nyima Basin, and the tectonic evolution mechanism of the Nyima Basin was analyzed from a microscopic perspective. According to the sedimentary magnetic fabric and strained magnetic fabric of the red layer, combined with the observation under the mineral microscope, the rock magnetic experiment and the zircon U-Pb dating study, we obtained the following conclusions:

(1) In the Jingzhushan Formation of the Late Cretaceous from the Nyima Basin, the magnetic susceptibility of the red-bed sandstone is controlled by paramagnetic mica minerals. The magnetic minerals in the northern sampling point are mainly quartz, chlorite and sericite; The magnetic minerals in the southern sampling point are white mica, biotite and chlorite. Samples with average values of magnetic susceptibility greater than 500×10^{-6} SI may have ferromagnetic minerals added, such as magnetite and hematite. There are more magnetic minerals in the southern samples than in the northern samples.

(2) There are strained magnetic fabrics developed at the sampling points in the northern Nyima Basin, including tensile lineation fabric and pencil-like fabric, reflecting the extrusion stress of SE-NW at 298.4°. The structure is dominated by the thrust of the SW disk, accompanied by a certain right strike-slip. Sedimentary magnetic fabric is developed in the southern sampling point, showing bidirectional paleocurrents.

(3) The zircon U-Pb dating of the volcanic rocks in the Jingzhushan Formation from the Coqen Basin is about 92 Ma, which is consistent with the Nyima Basin. Studies of provenance comparison show that the age of the Jingzhushan formation in the Nyima Basin

is similar to that of the South Qiangtang Block and the North Lhasa Block. The provenance of the Nyima Basin may be from both sources.

(4) The Nyima Basin of the Jingzhushan Formation in the Late Cretaceous was formed under the tectonic background with the northward subduction by the Natmso-Shiquan River small oceanic basin and the southward subduction by the Bangong-Nujiang residual oceanic basin. There was an arc-arc "soft collision" of the arc-basin system between the Shiquan River-Namtso oceanic basin and Bangong-Nujiang Tethys Oceanic Basin. Compared with the Bangong-Nujiang Tethys Ocean, the Nyima Basin belongs to the back-arc foreland basin in an ocean-continent type.

Author Contributions: Conceptualization, Q.C.; methodology, N.J.; software, B.W. (Bitian Wei) and D.Z.; validation, F.H. and Y.L.; formal analysis, Y.Z.; investigation, Y.Z.; resources, B.W. (Bitian Wei), P.X., T.L., F.L., L.X., J.W. (Jingyue Wu) and J.W. (Jiawei Wang); data curation, X.C.; writing—original draft preparation, Q.C.; writing—review and editing, Q.C.; visualization, visualization; supervision, H.W.; project administration, H.W.; funding acquisition, H.W. All authors have read and agreed to the published version of the manuscript.

Funding: This research was funded by [the National Natural Science Foundation of China] grant number [41774073, 91855211, 42074075, and 41304049] And The APC was funded by [the Second Tibetan Plateau Scientific Expedition (STEP) program] grant number [2019QZKK0704]. Information regarding the funder and the funding number should be provided.

Data Availability Statement: The data used for writing of this article are all presented in the article.

Acknowledgments: Thanks to three anonymous reviewers and editors for their help.

Conflicts of Interest: The authors declare no conflict of interest.

References

1. Harrison, T.M.; Copeland, P.; Kidd, W.S.F.; Yin, A. Rasing Tibet. *Science* **1992**, *255*, 1663–1670. [CrossRef] [PubMed]
2. Tappommier, P.; Xu, Z.Q.; Roger, F.; Meyer, B.; Arnaud, N.; Wittlinger, G.; Yang, J.S. Oblique stepwise rise and growth of the Tibet Plateau. *Science* **2001**, *294*, 1671–1677. [CrossRef]
3. Zhu, L.D.; Wang, C.S.; Zheng, H.B.; Xiang, F.; Yi, H.S.; Liu, D.Z. Tectonic and sedimentary evolutions of basins in the northeast of Qinghai-Tibet Plateau and their implications for the northward growth of the Plateau, Paleogeography. *Paleoclimatology Paleoecol.* **2006**, *241*, 49–60. [CrossRef]
4. Wang, C.Y.; Han, W.B.; Wu, J.P.; Lou, H.; Winston Chan, W. Crustal structure beneath the eastern margin of the Tibetan Plateau and its tectonic implications. *J. Geophys. Res.* **2007**, *112*, B07307. [CrossRef]
5. Pan, G.T.; Wang, L.Q.; Li, R.S.; Yuan, S.H.; Ji, W.H.; Yin, F.G.; Zhang, W.P.; Wang, B.D. Tectonic evolution of the Qinghai-Tibet Plateau. *J. Asian Earth Sci.* **2011**, *53*, 3–14. [CrossRef]
6. Xia, L.Q.; Li, X.M.; Ma, Z.P.; Xu, X.Y.; Xia, Z.C. Cenozoic volcanism and tectonic evolution of the Tibetan plateau. *Gondwana Res.* **2011**, *19*, 850–866. [CrossRef]
7. Zhang, Y.C.; Shi, G.R.; Shen, S.Z. A review of Permian stratigraphy, paleobiogeography and paleogeography of the Qinghai-Tibet Plateau. *Gondwana Res.* **2012**, *24*, 55–76. [CrossRef]
8. Zhang, K.J.; Zhang, Y.X.; Tang, X.C.; Xia, B. Late Mesozoic tectonic evolution and growth of the Tibetan plateau prior to the Indo-Asian collision. *Earth-Sci. Rev.* **2012**, *114*, 236–249. [CrossRef]
9. Soesoo, A.; Bons, P.D.; Gray, D.R. Divergent double subduction: Tectonic and petrologic consequences. *Geology* **1997**, *25*, 755–758. [CrossRef]
10. Gao, R.; Li, P.W.; Li, Q.S.; Guan, Y.; Shi, D.N.; Kong, X.R.; Liu, H.B. Deep process of the collision and deformation on the northern margin of the Tibetan Plateau: Revelation from investigation of the deep seismic profiles. *Sci. China Ser. D Earth Sci.* **2001**, *44*, 71–78. [CrossRef]
11. Zhu, D.C.; Zhao, Z.D.; Niu, Y.L.; Dilek, Y.; Hou, Z.Q.; Mo, X.X. The origin and pre-Cenozoic evolution of the Tibetan Plateau. *Gondwana Res.* **2013**, *23*, 1429–1454. [CrossRef]
12. Tang, L.J.; Huang, T.Z.; Jin, W.Z.; Lu, Z.Z.; He, C.B.; Ning, F.; Wang, P.H.; Chen, Q. Differential deformation and hydrocarbon accumulation in the Superimposed Basins. *Earth Sci. Front.* **2009**, *16*, 13–22. [CrossRef]
13. Alcicek, M.C.; Brogi, A.; Capezzuoli, E.; Liotta, D.; Meccheri, M. Superimposed basin formation during Neogene-Quaternary extensional tectonics in SW-Anatolia (Turkey): Insights from the kinematics of the Dinar Fault Zone. *Tectonphysics* **2013**, *608*, 713–727. [CrossRef]
14. Zhu, D.C.; Li, S.M.; Cawood, P.A.; Wang, Q.; Zhao, Z.D.; Liu, S.A.; Wang, L.Q. Assembly of the Lhasa and Qiangtang terranes in central Tibet by divergent double subduction. *Lithos* **2016**, *245*, 7–17. [CrossRef]
15. Badham, J.P.D. Strike-slip orogens-an explanation for the Hercynides. *J. Geol. Soc.* **1982**, *139*, 493–504. [CrossRef]

16. Waldron, J.W.F. Extensional fault arrays in strike-slip and transtension. *J. Struct. Geol.* **2005**, *27*, 23–34. [CrossRef]
17. Pascucci, V.; Costantini, A.; Peter Martini, I.; Dringoli, R. Tectono-sedimentary analysis of a complex, extensional, Neogene basin formed on thrust-faulted, Northern Apennines hinterland: Radicofani Basin, Italy. *Sediment. Geol.* **2005**, *183*, 71–97. [CrossRef]
18. Deng, H.W.; Wang, R.J.; Xiao, Y.; Guo, J.Y.; Xie, X.J. Tectono-Sequence stratigraphic analysis in continental faulted basins. *Earth-Sci. Front.* **2008**, *15*, 1–7. [CrossRef]
19. Stone, P.; Floyd, J.D.; Barnes, R.P.; Lintern, B.C. A sequential back-arc and foreland basin thrust duplex model for the Southern Uplands of Scotland. *J. Geol. Soc.* **1987**, *144*, 753–764. [CrossRef]
20. McAtamney, J.; Klepeis, K.; Mehrtens, C.; Thomson, S.; Betka, P.; Rojas, L.; Snyder, S. Along-strike variability of back-arc basin collapse and the initiation of sedimentation in the Magallanes foreland basin, southernmost Andes(53–54.5° S). *Tectonics* **2011**, *30*, TC5001. [CrossRef]
21. Borradaile, G.J.; Alford, C. Experimental shear zones and magnetic fabrics. *J. Struct. Geol.* **1988**, *10*, 895–904. [CrossRef]
22. Housen, B.A.; Richter, C.; van der Pluijm, B.A. Composite magnetic anisotropy fabrics: Experiments, numerical models and implications for the quantification of rock fabrics. *Tectonophysics* **1993**, *220*, 1–12. [CrossRef]
23. Aranguren, A.; Cuevas, J.; Tubia, M.J. Composite magnetic fabrics from S-G mylonites. *J. Struct. Geol.* **1996**, *18*, 863–869. [CrossRef]
24. Pares, J.M.; van der Pluijm, B.A.; Dinares-Turell, J. Evolution of magnetic fabrics during incipient deformation of mudrocks (Pyrenees, northern Spain). *Tectonophysics* **1999**, *307*, 1–14. [CrossRef]
25. Ferre, E.C.; Gebelin, A.; Jessica, L.T.; Sassier, C.; Burmeister, K.C. Deformation and magnetic fabrics in ductile shear zones: A review. *Tectonophysics* **2014**, *629*, 179–188. [CrossRef]
26. Gurioli, L.; Pareschi, M.T.; Zanella, E.; Lanza, R.; Deluca, E.; Bisson, M. Interaction pyroclastic density currents with human settlements: Evidence from ancient Pompeii. *Geology* **2005**, *33*, 441–444. [CrossRef]
27. Cifelli, F.; Ballato, P.; Alimohammadian, H.; Sabour, J.; Mattei, M. Tectonic magnetic lineation and oroclinal bending of the Alborz range: Implications on the Iran-Southern Caspian geodynamics. *Tectonics* **2015**, *34*, 116–132. [CrossRef]
28. Zhong, L.L.; Zhong, K.H.; Qin, Q. Structural characteristics of the Nima Basin in the Bangong-Nujiang tectonic belt, central Tibet. *Earth Sci. Front.* **2021**, *29*, 266–284.
29. Decelles, P.G.; Kapp, P.; Ding, L.; Gehrels, G.E. Late Cretaceous to middle Tertiary basin evolution in the central Tibetan Plateau: Changing environments in response to tectonic partitioning, aridification, and regional elevation gain. *GSA Bull.* **2009**, *119*, 654–680. [CrossRef]
30. Girdler, R.W. The measurement and computation of anisotropy of magnetic susceptibility of rocks. *Geophys. J. Int.* **1961**, *5*, 34–44. [CrossRef]
31. Jelinek, V. Characterization of the magnetic fabric of rocks. *Tectonophysics* **1981**, *79*, 63–67. [CrossRef]
32. Tarling, D.H.; Hrouda, F. *The Magnetic Anisotropy of Rocks*; Chapman & Hall: London, UK, 1993; pp. 1–189.
33. Stacey, F.D.; Joplin, G.; Lindsay, J. Magnetic anisotropy and fabric of some foliated rocks from S.E. Australia. *Geofis. Pura E Appl.* **1960**, *47*, 30–40. [CrossRef]
34. Liang, W.T.; Zhang, G.W.; Yu, B.; Lu, R.K.; Pei, X.Z.; Jin, C.S. Magnetic fabric study and its tectonic significance of suture zones in joint area of Qinling and Qilianshan. *Chin. J. Geophys.* **2009**, *52*, 85–94. [CrossRef]
35. Hrouda, F. Magnetic anisotropy of rocks and its application in geology and geophysics. *Geophys. Surv.* **1982**, *5*, 37–82. [CrossRef]
36. Li, B.L.; Fan, H.B.; Zhu, D.Q.; Peng, B.; Guo, P.; Zhou, L.; Li, Y.F. Geochemical characteristics, detrital zircon U-Pb geochronology, and its tectonic significance for the Jingzhushan Formation from northern region of Geji County, northern Tibet. *Acta Geol. Sin.* **2020**, *94*, 3658–3673.
37. Masher, B.A. Magnetic properties of some synthetic sub-micron magnetites. *Geophys. J. Int.* **1988**, *94*, 83–96. [CrossRef]
38. Hrouda, F.; Jelinek, V. Resolution of ferrimagnetic and paramagnetic anisotropies in rocks, using combined low-field and high-field measurements. *Geophys. J. Int.* **1990**, *103*, 75–84. [CrossRef]
39. Dekkers, M.J. Magnetic properties of natural pyrrhotite Part I: Behavior of initial susceptibility and saturation-magnetization-related rock-magnetic parameters in a grain-size dependent framework. *Phys. Earth Planet. Inter.* **1988**, *52*, 376–393. [CrossRef]
40. Liu, Y.C.; Zhou, Y.N.; Cheng, X.; Ye, Y.K.; Wei, B.T.; Jiang, N. Paleomagnetism of the Late Cretaceous Jingzhushan Formation red beds on the northern margin of the Lhasa terrane in the Qinghai-Tibet Plateau and its tectonic significance. *Prog. Geophys.* **2022**, *39*, e2020TC006280.
41. Borradaile, G.J.; Henry, B. Tectonic applications of magnetic susceptibility and its anisotropy. *Earth-Sci. Rev.* **1997**, *42*, 49–93. [CrossRef]
42. Gehrels, G.; Kapp, P.; Decelles, P.; Pullen, A.; Blakey, A.; Weislogel, A.; Ding, L.; Guynn, J.; Martin, A.; McQuarrie, N.; et al. Detrital zircon geochronology of pre-Tertiary strata in the Tibetan-Himalayan orogen. *Tectonics* **2011**, *30*, TC5016. [CrossRef]
43. Rochette, P. Magnetic susceptibility of the rock matrix related to magnetic fabric studies. *J. Struct. Geol.* **1987**, *9*, 1015–1020. [CrossRef]
44. Borradaile, G.J.; Jackson, M. Anisotropy of magnetic susceptibility (AMS): Magnetic petrofabrics of deformed rocks. *Geol. Soc.* **2004**, *238*, 299–360. [CrossRef]
45. Cao, X.W.; Sun, Z.M.; Huang, B.C. Magnetic fabric separation and analysis of rock tectonic deformation. *Chin. J. Geophys.* **2022**, *65*, 448–470.
46. Jia, D.; Chen, Z.X.; Luo, L.; Hu, Q.W.; Jia, Q.P.; Li, Y.Q. Magnetic fabric and finite strain in fault-related folds: Case analysis of Mianjiang thrust structure in Western Sichuan. *Prog. Nat. Sci.* **2007**, *17*, 188–195.

47. He, X.; Shen, Q.; Jiang, K.; Li, C.Z.; Wu, G.Z.; Ran, Y.Z.; Jin, C.S.; Liang, W.T. Room and low temperature magnetic fabrics of fine-grained clastic rocks: A case study of the Cretaceous Huicheng basin, Qingling orogen. *Chin. J. Geophys.* **2022**, *65*, 737–753.
48. Borradaile, G.J.; Hamilton, T. Magnetic fabrics may proxy as neotectonic stress trajectories, Polis rift, Cyprus. *Tectonics* **2004**, *23*, TC1001. [CrossRef]
49. Engelder, T.; Geiser, P. The relationship between pencil cleavage and lateral shortening within the Devonian section of the Appalachian Plateau, New York. *Geology* **1979**, *7*, 460–464. [CrossRef]
50. Luo, L.; Jia, D.; Qi, J.F. Magnetic fabrics investigation in Tianquan-Leshan section in front of Longmenshan fold-thrust belt and its indicative significance for the Cenozoic deformation. *Chin. J. Geophys.* **2013**, *56*, 558–566.
51. Wang, K.; Jia, D.; Luo, L. Magnetic fabric and structural deformation. *Chin. J. Geophys.* **2017**, *60*, 1007–1026.
52. Wu, H.N. Magnetic fabric of rock and its application in analysis of rock deformation. *Acta Petrol. Sin.* **1988**, *52*, 2588–2594.
53. Zhu, D.C.; Pan, G.T.; Chung, S.L.; Liao, Z.L.; Wang, L.Q.; Li, G.M. Shrimp zircon age and geochemical constraints on the origin of Lower Jurassic volcanic rocks from the Yeba Formation, Southern Gandses, South Tibet. *Int. Geol. Rev.* **2008**, *50*, 442–471. [CrossRef]
54. Ye, P.S.; Wu, Z.H.; Hu, D.G.; Jiang, W.; Yang, X.D. Geochemical characteristic of Ophiolite in Yongzhu-Guomangcuo, Tibet and its tectonic significance. *Eng. Geol. Environ. Geol. (Geosci.)* **2005**, *19*, 508–514.
55. Dickinson, W.R. Interpreting Provenance Relations from Detrital Modes of Sandstones. In *Provenance of Arenites*; Springer: Dordrecht, The Netherlands, 1985; Volume 148, pp. 333–361.
56. Li, X.K.; Chen, J.; Wang, R.C.; Li, C.; Wang, M.; Liu, J.H.; Yu, Y.P.; Luo, B.A. Early Cretaceous tectonomagmatic evolution and basin development of western Bangong-Nujiang suture: A complete history of soft collision. *Lithos* **2019**, *344–345*, 360–373. [CrossRef]
57. Song, S.G.; Niu, Y.L.; Wei, C.J.; Ji, J.Q.; Su, L. Metamorphism, anatexis, zircon ages and tectonic evolution of the Gongshan block in the northern Indochina continent-An eastern extension of the Lhasa Block. *Lithos* **2010**, *120*, 327–346. [CrossRef]
58. Zhu, D.C.; Zhao, Z.D.; Niu, Y.L.; Mo, X.X.; Chuang, S.L.; Hou, Z.Q.; Wang, L.Q.; Wu, F.Y. The Lhasa Terrane: Record of a microcontinent and its histories of a drift and growth. *Earth Planet. Sci. Lett.* **2011**, *301*, 241–255. [CrossRef]
59. Zhu, D.C.; Zhao, Z.D.; Niu, Y.L.; Dilek, Y.; Mo, X.X. Lhasa terrane in southern Tibet came from Australia. *Geology* **2011**, *39*, 727–730. [CrossRef]
60. Hao, J.; Zhai, M.G. Jinning Movement and Sinian System in China: Their relationship with Rodina Supercontinent. *Chin. J. Geol.* **2004**, *3*, 139–152.
61. Liu, W.; Wu, J.L.; Lei, C.Y.; Wang, B.; Lang, X.H. Detrital zircon geochronology of the Shamuluo Formation in Geji region of central Tibet: Provenance and evidence for the closure time of the Bangong Co-Nujiang Tethys Ocean. *Acta Petrol. Sin.* **2019**, *35*, 1738–1756.
62. Pan, G.T.; Mo, X.X.; Hou, Z.Q.; Zhu, D.C.; Wang, L.Q.; Li, G.M.; Zhao, Z.D.; Geng, Q.R.; Liao, Z.L. Spatial-temporal framework of the Gangdese Orogenic Belt and its evolution. *Acta Petrol. Sin.* **2006**, *22*, 521–533.